Available online at www.sciencedirect.com

ScienceDirect

Geochimica et Cosmochimica Acta 320 (2022) 179–206

Geochimica et Cosmochimica Acta

www.elsevier.com/locate/gca

Sulfide enrichment along igneous layer boundaries in the lower oceanic crust: IODP Hole U1473A, Atlantis Bank, Southwest Indian Ridge

Bartosz Pieterek [a], Jakub Ciazela [b,*], Marine Boulanger [c], Marina Lazarov [d], Anna V. Wegorzewski [e], Magdalena Pańczyk [f], Harald Strauss [g], Henry J.B. Dick [h], Andrzej Muszyński [a], Juergen Koepke [d], Thomas Kuhn [e], Zbigniew Czupyt [f], Lydéric France [c]

[a] *Institute of Geology, Adam Mickiewicz University, ul. Bogumiła Krygowskiego 12, 61-680 Poznań, Poland*
[b] *Institute of Geological Sciences, Polish Academy of Sciences, ul. Twarda 51/55, 00-818 Warsaw, Poland*
[c] *Université de Lorraine, CNRS, CRPG, 15 rue Notre Dame des Pauvres BP 20, 54500 Vandœuvre les Nancy, France*
[d] *Institute of Mineralogy, Leibniz University of Hannover, Callinstr. 3, 30167 Hannover, Germany*
[e] *Federal Institute for Geosciences and Natural Resources (BGR), Stilleweg 2, D-30655 Hannover, Germany*
[f] *Polish Geological Institute – National Research Institute, ul. Rakowiecka 4, Warszawa 00-975, Poland*
[g] *Institut für Geologie und Paläontologie, Westfälische Wilhelms-Universität Münster, Corrensstr. 24, D-48149 Münster, Germany*
[h] *Department of Geology and Geophysics, Woods Hole Oceanographic Institution, MS #8, McLean Laboratory, Woods Hole, MA 02543-1539, USA*

Received 22 March 2021; accepted in revised form 6 January 2022; available online 12 January 2022

Abstract

Reactive porous or focused melt flows are common in crystal mushes of mid-ocean ridge magma reservoirs. Although they exert significant control on mid-ocean ridge magmatic differentiation, their role in metal transport between the mantle and the ocean floor remains poorly constrained. Here we aim to improve such knowledge for oceanic crust formed at slow-spreading centers (approximately half of present-day oceanic crust), by focusing on specific igneous features where sulfides are concentrated. International Ocean Discovery Program (IODP) Expedition 360 drilled Hole U1473A 789 m into the lower crust of the Atlantis Bank oceanic core complex, located at the Southwest Indian Ridge. Coarse-grained (5–30 mm) olivine gabbro prevailed throughout the hole, ranging locally from fine- (<1 mm), to very coarse-grained (>30 mm). We studied three distinct intervals of igneous grain size layering at 109.5–110.8, 158.0–158.3, and 593.0–594.4 meters below seafloor to understand the distribution of sulfides. We found that the layer boundaries between the fine- and coarse-grained gabbro were enriched in sulfides and chalcophile elements. On average, sulfide grains throughout the layering were composed of pyrrhotite (81 vol.%; $Fe_{1-x}S$), chalcopyrite (16 vol.%; $CuFeS_2$), and pentlandite (3 vol.%; $[Ni,Fe,Co]_9S_8$), which reflect paragenesis of magmatic origin. The sulfides were most commonly associated with Fe-Ti oxides (titanomagnetites and ilmenites), amphiboles, and apatites located at the interstitial positions between clinopyroxene, plagioclase, and olivine. Pentlandite exsolution textures in pyrrhotite indicate that the sulfides formed from high-temperature sulfide liquid separated from mafic magma that exsolved upon cooling. The relatively homogenous phase proportion within sulfides along with their chemical and isotopic compositions throughout the studied intervals further support the magmatic origin of sulfide enrichment at the layer boundaries. The studied magmatic layers were likely formed as a result of intrusion of more primitive magma (fine-grained gabbro) into the former crystal mush (coarse-grained gabbro). Sulfides from the coarse-grained gabbros are Ir-Platinum Group Element-rich (PGE;

* Corresponding author.
E-mail address: j.ciazela@twarda.pan.pl (J. Ciazela).

https://doi.org/10.1016/j.gca.2022.01.004
0016-7037/© 2022 The Authors. Published by Elsevier Ltd.
This is an open access article under the CC BY-NC-ND license (http://creativecommons.org/licenses/by-nc-nd/4.0/).

i.e., Ir, Os, Ru) but those from the fine-grained gabbros are Pd-PGE-rich (i.e., Pd, Pt, Rh). Notably, the sulfides from the layer boundaries are also enriched in Pd-PGEs, and therefore elevated sulfide contents at the boundaries were likely related to the new intruding melt. Because S concentration at sulfide saturation level is dependent on the Fe content of the melt, sulfide crystallization may have been caused by FeO loss, both via crystallization of late-precipitating oxides at the boundaries, and by exchange of Fe and Mg between melt and Fe-bearing silicates (olivine and clinopyroxene). The increased precipitation of sulfide grains at the layer boundaries might be widespread in the lower oceanic crust, as also observed in the Semail ophiolite and along the Mid-Atlantic Ridge. Therefore, this process might affect the metal budget of the global lower oceanic crust. We estimate that up to ~20% of the Cu, ~8% of the S, and ~84% of the Pb of the oceanic crust inventory is accumulated at the layer boundaries only from the interaction between crystal mush and new magma.
© 2022 The Authors. Published by Elsevier Ltd. This is an open access article under the CC BY-NC-ND license (http://creativecommons.org/licenses/by-nc-nd/4.0/).

Keywords: Sulfides; Chalcophile elements; Platinum group elements; Lower oceanic crust; IODP

1. INTRODUCTION

The well-known Penrose model of the oceanic crust (Conference participants, 1972) predicts a uniform and 6–7-km thick oceanic crust, based on the studies of the obducted oceanic lithosphere (e.g., western United States and European ophiolites including Troodos and Coast Range Ophiolites), and geophysical surveys through the oceanic lithosphere in present-day oceans. In this model, the crystalline part of the oceanic crust is assumed to be well stratified into three layers: basaltic lavas, sheeted dikes, and gabbros, which show a planar boundary with the underlying peridotites of the upper mantle, topped by a dunite-rich layer (Dilek, 2003). Geochemical models of chalcophile element migration and distribution in the oceanic crust are based on the Penrose ocean crust stratigraphy that assumes MORB differentiation controlled mostly by fractional crystallization (Klein, 2003; Jenner et al., 2010; Jenner and O'Neill, 2012). However, these models are limited only to the idealized, fast-spreading, crust that has not been overprinted by other processes (Dick et al., 2006). Many studies, especially on slow-spreading ridges, indicate heterogeneity of the oceanic lithosphere not predicted by the Penrose model (Cannat, 1996; Blackman and Collins, 2010). Moreover, a significant reduction of the thickness of the oceanic crust is observed in many locations along slow-spreading ridges (Bonatti et al., 2003; Escartín et al., 2008; Ciazela et al., 2015). Heterogeneous and thinner oceanic crust implies a more important role of melt-rock reaction with respect to fractional crystallization during magma differentiation in the lower oceanic crust (Coogan et al., 2000b; Koepke et al., 2005; Lissenberg and Dick, 2008; Boulanger et al., 2020; Sanfilippo et al., 2020; Ferrando et al., 2021a, 2021b).

To date, attempts to understand sulfide behavior during melt-rock reactions have been made only for melt-mantle reactions in the crust-mantle boundary and upper mantle. For example, at the Kane Megamullion oceanic core complex (OCC), Ciazela et al. (2018) found an enrichment in chalcophile metals at the crust-mantle transition zone and interpreted this enrichment as related to the crystallization of sulfides during extensive melt-mantle reaction throughout this horizon of the oceanic lithosphere. Similarly, González-Jiménez et al. (2020a) described magmatic sulfides hosted by a chromite deposit at the crust-mantle transition zone of the Moa-Baracoa ophiolite in eastern Cuba. The local sulfides in Cuba are magmatic in origin and most likely related to an interaction between migrating volatile-rich mafic melts and the chromitite at the crust-mantle transition zone of the oceanic lithosphere. In both aforementioned studies, the crystallization of sulfides during melt-rock reactions could have been related to the loss of iron from the melt. Although these two studies and others (Zhou et al., 1996; Zhou et al., 2001; Sanfilippo et al., 2016; González-Jiménez et al., 2020b), revealed that melt-rock reaction between mid-oceanic ridge basalt (MORB)-like melt and mantle peridotites strongly affects the metal budget of the upper mantle and oceanic crust, less is known on how metals behave during melt-rock reaction within the lower oceanic crust. Considering that the typical MORB-like melts are expected to contain 100–120 ppm Cu (Jenner and O'Neill, 2012; Lee et al., 2012; Jenner, 2017) and dikes with lavas contain on average 72–81 ppm Cu (Engel et al., 1965; Hamlyn et al., 1985; Doe, 1994; White and Klein, 2013), lower crustal rocks (a ratio of 1:2 between dikes with lavas, and gabbro cumulates) should contain from 109.5 to 144 ppm Cu to compensate the discrepancy between the sulfide-bearing lower crustal rocks and overlying dikes with lavas (Li, 2014; Ciazela et al., 2017). However average lower crustal cumulates are reported to contain 71 ± 19 ppm Cu (Coogan, 2014). This discrepancy has been already highlighted by Jenner (2017), Ciazela et al. (2017, 2018), and Wang et al. (2018) and implies that a certain portion of the Cu may be accumulated either at the upper mantle and at the crust-mantle transition, or other hitherto unsampled locations in the lower crust. However, aforementioned studies did not fully explain the Cu deficit for the whole lower crust. Here we explore whether narrow intrusive zones of melt-rock reaction are the location of missing chalcophile elements.

In the lower oceanic crust, intrusive layers with sulfide enrichment on their boundaries have been found in the fast-spreading systems. Lachize et al. (1991) and Lorand and Juteau (2000) described magmatic sulfide-rich zones (pyrrhotite-pentlandite-chalcopyrite assemblages) hosted

by layered gabbros in the Wadi Haymiliyah (Haylyn Block, Semail Ophiolite, Oman). These sulfides were concentrated both within the fine-grained gabbro and along their boundaries with the coarse-grained domain. In addition, Boudier et al. (2000) found enhanced sulfide precipitation associated with microgranular gabbronoritic layers that were interlayered with olivine-gabbro. These gabbronoritic layers likely represent stoped hydrothermally altered dike pieces transposed by the downward magmatic flow of the gabbro (Boudier et al., 2000; France et al., 2009; Nicolas et al., 2009). Enhanced sulfide contents are present both within the gabbronorite layers and at the contacts between the gabbronorite and olivine-gabbro. Considering the primary magmatic sulfide ores hosted by layered gabbros within Semail ophiolite representing oceanic crust formed at fast-spreading settings, it seems fruitful to investigate similar igneous features that might occur at slow-spreading ridges and accumulate the certain portion of chalcophile metals. The aforementioned observations are not yet systematic but suggest that narrow zones of igneous layering are worth of examining, in terms of sulfide distribution and metal behavior.

In the slow-spreading lower oceanic crust there are some evidences on sulfide enrichment at layer boundaries. For example sulfides, S, and selected chalcophile metals (Cu, Ni) have been investigated at 1508-m deep Hole 735B at Atlantis Bank OCC (32°43′S, 57°16′E) along the Southwest Indian Ridge (SWIR) (Alt and Anderson, 1991; Miller and Cervantes, 2002). These sulfides are clearly of magmatic origin and are commonly observed at the boundaries between fine-grained and coarse-grained gabbro (Miller and Cervantes, 2002). In another deep IODP hole sampling the lower crust, the 1415-m deep Hole U1309D on the Atlantis Massif OCC (30°N along the Mid-Atlantic Ridge; MAR), interlayered gabbros of highly variable grain size and modal mineralogy have been recovered (Expedition 304/305 Scientists, 2006; Ildefonse et al., 2006; Castelain et al., 2014). These rocks display downhole geochemical variations indicating formation by multiple magma injections (Godard et al., 2009). They mostly show mantle source S isotope signatures (from −1.2‰ to +0.7‰) and consistent S contents (from 385 to 654 ppm) (Delacour et al., 2008), confirming the common presence of magmatic pyrrhotite-chalcopyrite-pentlandite assemblages. Based on core description (Expedition 304/305 Scientists, 2006), the sulfides are most abundant along the boundaries between the different grain size domains (e.g., 681.9–683.3 and 862.9–864.0 mbsf).

To provide constraints on sulfide and chalcophile metals enrichment documented at the igneous layer boundaries within the lower oceanic crust and to study the magmatic processes responsible for this enrichment, we investigated three representative igneous layering intervals discovered in the 809-m-deep Hole U1473A drilled into the gabbroic massif of the Atlantis Bank OCC (32°43′S, 57°17′E) along the SWIR during International Ocean Discovery Program (IODP) Expedition 360 (MacLeod et al., 2017). Here, layers of coarse-grained gabbro cut by fine-grained gabbro, and the boundaries between the two, have been documented during shipboard description (MacLeod et al., 2017; Boulanger et al., 2021). Our whole-rock and *in situ* analyses (Sections 5.1 and 5.3) reveal enrichment in sulfides at boundaries between fine-grained gabbro crystallized from relatively primitive and late melts, and coarse-grained gabbros crystallized from relatively evolved and early crystal mush. We discuss various melt-rock reaction-related mechanisms responsible for this enrichment (Section 5.3). Finally, we discuss the importance of these processes for Cu, S, and other metal budget in the global oceanic crust (Sections 5.4 and 5.5).

2. GEOLOGICAL SETTING AND PETROGENESIS OF THE STUDIED SAMPLES

2.1. The Atlantis Bank OCC

The Atlantis Bank OCC is located to the east of the Atlantis II Transform along the SWIR, forming the shallowest, and northernmost part, of an elevated transverse ridge (Fig. 1A). Approximately 12 million years ago, the rifting caused detachment faulting, which occurred in the zone of active diking beneath the rift valley (Baines et al., 2003), exposing a plutonic massif temporarily exhumed as an ocean island (Palmiotto et al., 2013). The OCC is dome-shaped, 40 km long in the N-S direction and 30 km wide in the W-E direction, with a 25 km^2 flat-topped wave-cut platform at ∼700 m below sea level (Fig. 1; Dick et al., 2016). The predominance of gabbroic rocks throughout the entire OCC was revealed by dredging, dives, and drilling (Dick et al., 2019a and references therein). The gabbroic rocks at the upper portion of the Atlantis Bank footwall have been recovered by Ocean Drilling Program (ODP) Legs 118, 176 and 179, as well as IODP Expeditions 360 and 362T, that yielded the Holes 735B (Shipboard Scientific Party, 1999c; Dick et al., 2002), 1105A (Shipboard Scientific Party, 1999b), and U1473A (Blum et al., 2017; MacLeod et al., 2017), respectively (Fig. 1B).

Olivine gabbro chemistry indicated that Holes U1473A and 735B drilled through three and five gabbroic masses, respectively, each 200 to 450 m thick, that most likely represent separate magmatic intrusive units (Boulanger et al., 2020). Each of these units is made up of finer centimeter- to decimeter-thick subunits that formed by intrusive and melt migration events (Dick et al., 2019b; Boulanger et al., 2020; Boulanger et al., 2021; Ferrando et al., 2021a, 2021b). The gabbroic rocks reveal a hybrid-origin, with early troctolitic to olivine gabbroic mushes that were percolated by late magmatic liquid compacted out of olivine gabbro intrusions, which were locally Fe-Ti-rich (Dick et al., 2000, 2019b; Boulanger et al., 2020; Zhang et al., 2020; Boulanger et al., 2021; Ferrando et al., 2021a, 2021b). The late interstitial Fe-Ti melts migrated either along shear zones or boundaries between younger (warmer) and older (cooler) domains due to the permeability difference (Dick et al., 2019b). The cooling rate was sufficiently low to expel the interstitial melt that accumulated to form patches or layers of younger undeformed gabbros (Dick et al., 2019b; Ferrando et al., 2021b).

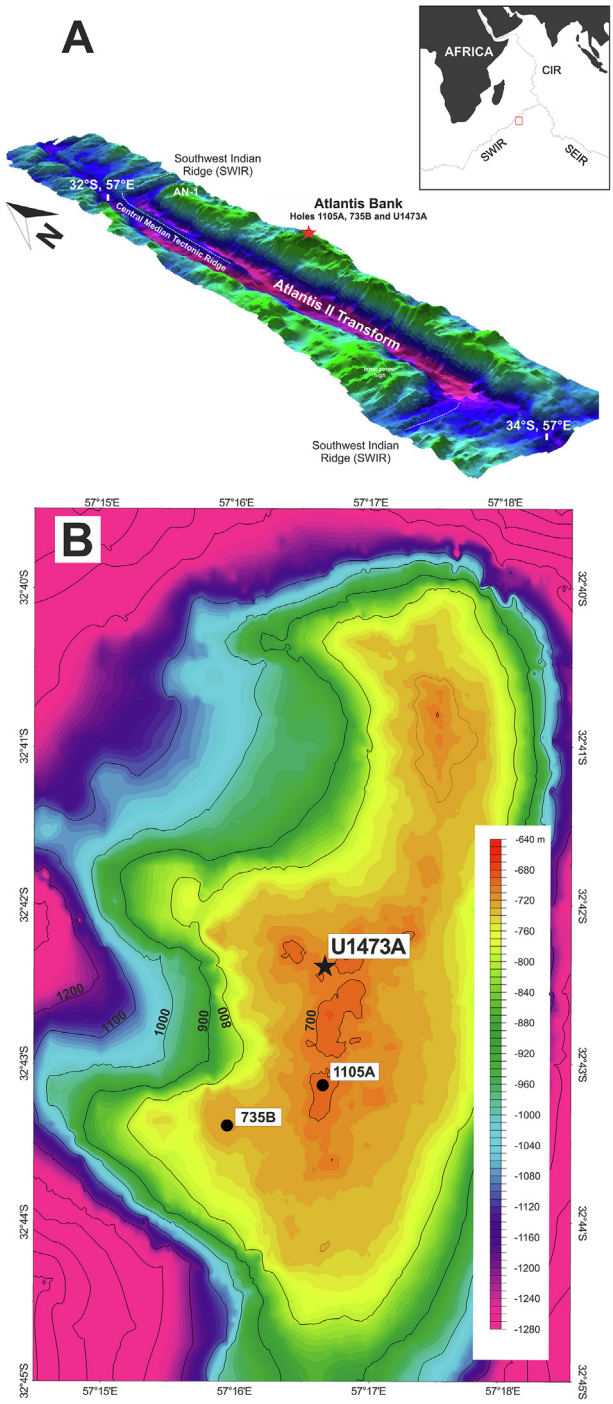

Fig. 1. (A) 3D bathymetry view of the Atlantis II Transform with the location of Atlantis Bank indicated, modified from Shipboard Scientific Party (1999a). The inset shows the position of Atlantis Bank along the Southwest Indian Ridge (SWIR). CIR – Central Indian Ridge. SEIR – Southeast Indian Ridge. (B) Bathymetry of the top plateau at Atlantis Bank modified from MacLeod et al. (2017).

2.2. Petrogenesis of the studied samples

The 809-m-deep Hole U1473A mostly recovered olivine gabbro (76.5 vol.%) and gabbro (14.6 vol.%) cumulate with minor oxide gabbro layers and patches (7.4 vol.%) (MacLeod et al., 2017). The gabbros were cut by generally subhorizontal or branched networks of felsic veins (remaining 1.5 vol.%) that vary in thickness from a few millimeters to several centimeters (MacLeod et al., 2017; Nguyen et al., 2018). Hole U1473A is dominated by moderately evolved olivine gabbro (Mg-number, defined as 100[molar Mg/(molar Mg + molar Fe)], ranging from 82 to 66; Dick et al., 2019b). The gabbroic rocks are mostly coarse-grained (5–30 mm), but in places fine- (<1 mm), medium- (1–5 mm), or very coarse-grained (>30 mm) (Figs. 2 and 3). Based on changes in igneous mineral modes, grain sizes, and textures, eight lithological units were defined (I–VIII; MacLeod et al., 2017). Igneous layering is especially well developed in Units II and VII. MacLeod et al. (2017) identified 195 layer boundaries in 67 series throughout the studied hole, 58 of which were in Unit II and 76 in Unit VII. Approximately 50% of igneous layers were limited by planar and subparallel boundaries (Boulanger et al., 2021), while the other ~50% represent centimeter-scale patches with irregular boundaries (Dick et al., 2017; MacLeod et al., 2017; Dick et al., 2019b; Ferrando et al., 2021a, 2021b). In this study, we will only focus on planar and subparallel boundaries within the two lithological Units II (91.3–175.0 mbsf) and VII (577.7–642.0 mbsf; MacLeod et al., 2017), where layering features have been shown to be particularly abundant. Within these two units, we investigated in detail three intervals at 109.5–110.8 (Section 13R-1), 158.0–158.3 (18R-1), and 593.0–594.4 mbsf (65R-5; Figs. 2 and S1) that reveal sharp and planar boundaries between fine- and coarse-grained domains.

Unit II is mostly represented by coarse-grained olivine gabbros containing medium- to fine-grained layers. The boundaries between different grain size domains within this unit, and among our samples, are mostly sub-planar and sharp (Fig. 2). Although the unit is locally affected by crystal-plastic deformation, centimeter-thick layers are present with sharp grain size and intrusive contacts. The sutured character of the boundaries between the fine- and coarse-grained gabbro suggests an intrusive origin of contacts (see Figs. 2, 3 and S2–S4; MacLeod et al., 2017). The Sections 13R-1 and 18R-1 investigated here are mostly undeformed. During the shipboard core description, interstitial sulfides along the contacts were observed (Fig. S5; MacLeod et al., 2017).

Unit VII is mostly composed of fine- to coarse-grained subophitic olivine gabbros that in places display grain size layering. In fact, this unit is characterized by the highest density of the layer boundaries in the entire hole (~1.4 boundary per meter; MacLeod et al., 2017). The contacts between the different grain size layers in most cases were sub-planar and subparallel to each other, but irregular boundaries were also found (MacLeod et al., 2017) and subdivided to sharp and diffusive (Ferrando et al., 2021b). These contacts were easily detectable mostly with the subparallel boundaries (Figs. 2 and S5). According to MacLeod et al. (2017) and Boulanger et al. (2021), Section 65R-5 records magmatic fabrics with foliation mostly parallel to the boundary between the layers (see also thin-section 65R-5-2.5/5 in Fig. S1).

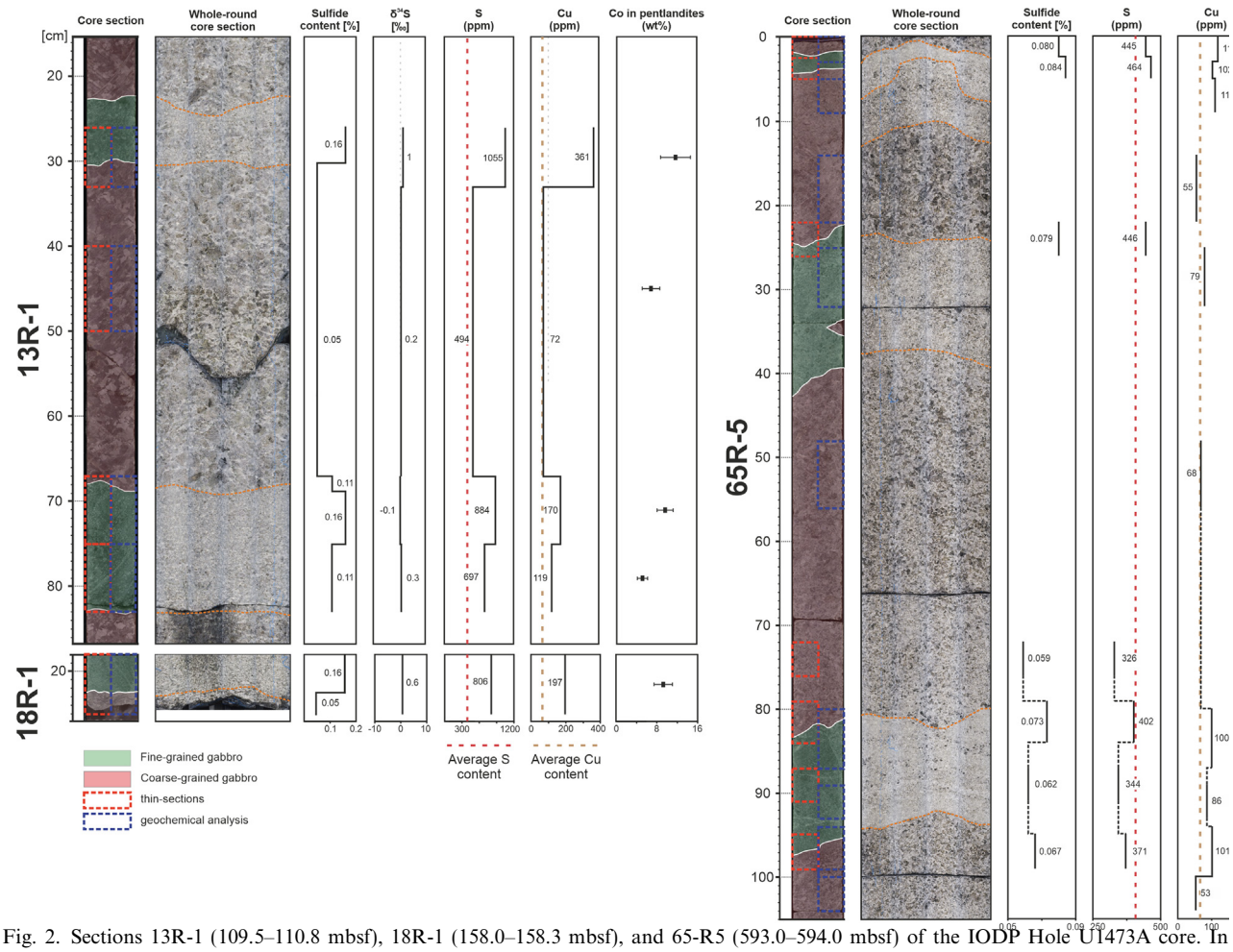

Fig. 2. Sections 13R-1 (109.5–110.8 mbsf), 18R-1 (158.0–158.3 mbsf), and 65-R5 (593.0–594.0 mbsf) of the IODP Hole U1473A core. In addition, we have presented the whole-rock core section photos, the logs of sulfide contents (based on SEM analysis for 13R-1 and 18R-1 as well as a petrographic description for 65R-5), whole-rock $S^{34}\delta$ signatures, whole-rock S and Cu contents (for more details see Section 3.2), and Co content of pentlandites in gabbros from the upper igneous layering intervals. Note that the igneous layering boundaries are enriched in whole-rock S and Cu as well as Co in pentlandites with respect to the coarse-grained and fine-grained gabbro. The $\delta^{34}S$ signature for upper intervals ranges between −0.1‰ and 1‰ indicating the mantle origin of S.

3. METHODS

3.1. Sample collection and preparation

We collected 12 samples for thin-sections (15 samples for whole-rock analyses) from the three igneous layering intervals, including 4 samples between 109.5 and 110.8 mbsf (Section 13R-1), 1 sample from 158.0–158.3 mbsf (Section 18R-1), and 7 samples (10 samples whole rock analyses; Fig. 2) from 593.0–594.4 mbsf (Section 65R-5) (see Figs. 2 and S1; Tables 1 and 3). The samples were cut out from the core using a diamond saw on board *JOIDES Resolution*. Initially, 13 thin-section billets (sample 13R-1-67-75 was duplicated) were cut out from the core to prepare 50-µm-thick polished thin-sections (see Figs. 2 and S1). The remainder, destined for whole-rock analyses, were carefully cleaned with a Hermes SiC sandpaper (grit size P120) to remove potential saw contamination. The samples were then washed three times in distilled water using an ultrasonic cleaner Sonorx Super RK for 10 min. Subsequently, samples were crushed using a Retsch BB51 tungsten carbide jaw crusher. Later, representative portions of the crushed materials were ground with a Siebtechnik agate swing mill for 4 min at a rotational speed of 710 rpm.

3.2. Petrographic description

Thin-sections were described under transmitted and reflected light using a Leica DM4 M optical microscope at the Institute of Mineralogy, Leibniz University of Hannover, Germany. The silicates contents were calculated based on the point-counting method while the sulfide contents were calculated by summing up individual areas of each identified sulfide grain and dividing that sum by the area of the thin-section (Fig. 2). We used the analogical method for determining the sulfides modes. The average sulfide modes were calculated by dividing the cumulative area of given sulfide phase by the total area of all sulfide phases in a studied thin-section (Table 1).

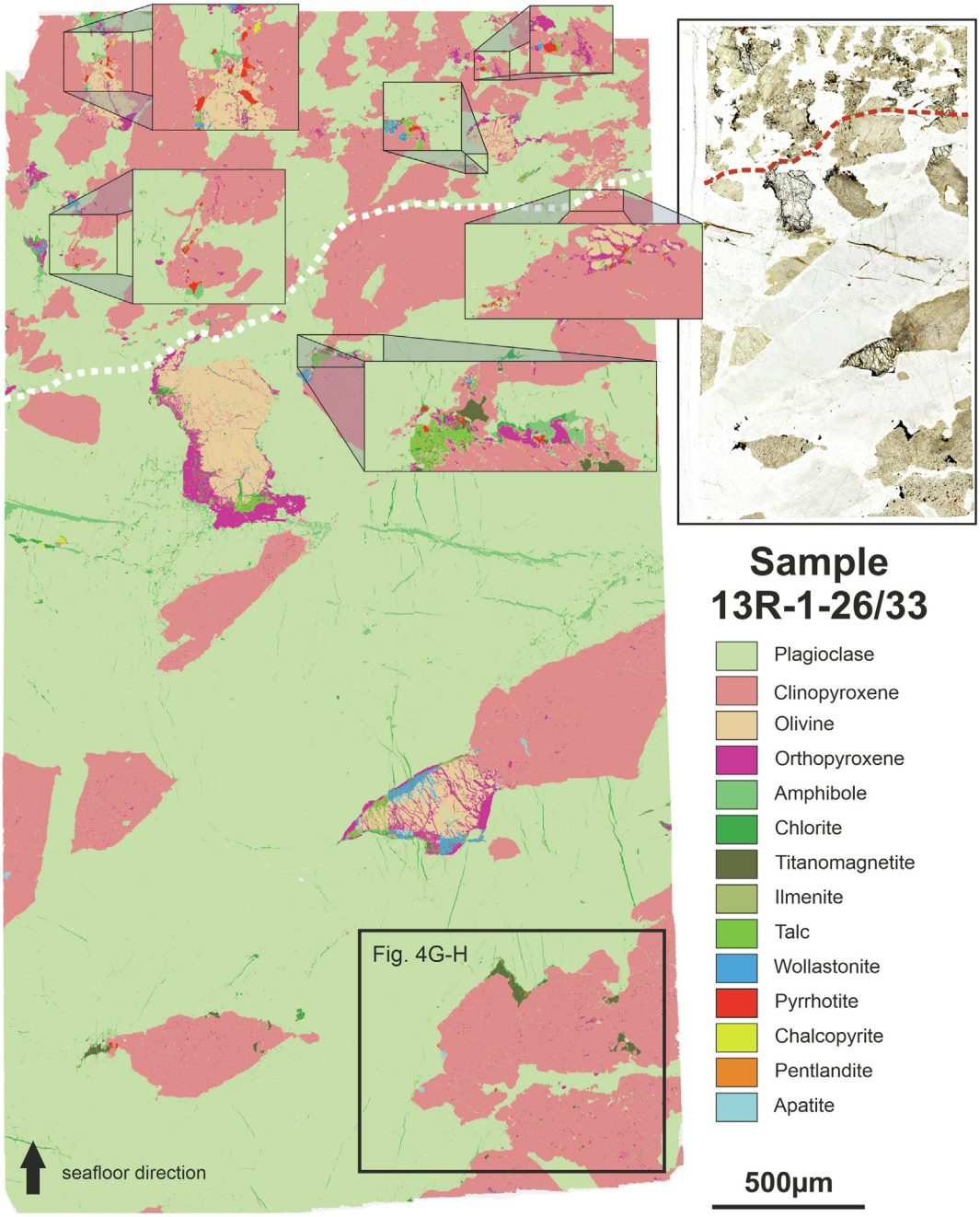

Fig. 3. Scanning electron microscopy mineral liberation analysis (SEM/MLA) showing the mineral distribution in Sample 13R-1-26/33 CIAZ representing the boundary zone sample with a contact between the coarse- and fine-grained gabbro (the white dotted line). Note that most sulfides (some are zoomed in the upper inserts) crystallized along the boundary zone between the coarse-grained and fine-grained gabbro. The black frame shows the location of the closeup image of the Fig. 4G and H. The minerals in the key are ordered according to decreasing abundance. The visible light image on the top right shows the same thin section with the same boundary marked in red.

3.3. Whole-rock analyses

The major element contents for the upper intervals (Sections 13R-1 and 18R-1) were determined using X-ray Fluorescence (XRF) spectroscopy at the Bundesanstalt für Geowissenschaften and Rohstoffe (BGR) in Hannover, Germany. First, 1 g of sample powder and 5 g $LiBO_2$ were mixed and melted for 20 min at 1200 °C to form tablets for analysis. The tablets were analyzed with a wavelength dispersive PANalytical AXIOS X-ray spectrometer equipped with a Rh X-ray tube. Calibration of the X-ray spectrometer was performed using a total of ~150 certified international reference materials (Table S1). The detection limits, and uncertainties for the whole-rock major element analysis are shown in Table S1, and certified standard materials used for calibration are included in Table S2. Data were automatically internally corrected for matrix effects and spectral interferences using the de Jongh method. The

Table 1
Characteristics of sulfides at the igneous layering intervals (109.5–110.8, 158.0–158.3, and 593.0–594.4 mbsf) from IODP Hole U1473A, Atlantis Bank.

Sample	Grain size[a]	Pyrrhotite[b]			Chalcopyrite			Pentlandite			Sulfides [vol.%] in opaque minerals
		Sulfide mode[c] [vol.%]	Maximum size [μm]	Typical size[d] [μm]	Sulfide mode[c] [vol.%]	Maximum size [μm]	Typical size[d] [μm]	Sulfide mode[c] [vol.%]	Maximum size [μm]	Typical size[d] [μm]	
13R-1-26/33[e]	Fine-grained	84	370	305	12	120	90	4	30	20	25
	Coarse-grained	78	200	170	20	250	85	2	30	15	20
13R-1-40/50[e]	Coarse-grained	90	400	350	9	150	100	1	50	40	25
13R-1-67/75A[e]	Coarse-grained	90	1000	500	9	700	345	1	30	25	25
	Fine-grained	81	150	100	18	75	45	1	15	12	30
13R-1-67/75B	Coarse-grained	87	1000	500	12	500	250	1	100	50	30
	Fine-grained	80	200	140	18	80	50	2	30	10	35
13R-1-75/83[e]	Fine-grained	89	400	300	10	100	95	1	25	15	35
18R-1-18/25	Fine-grained	82	350	240	16	100	70	2	60	60	30
	Coarse-grained	86	400	250	13	90	60	1	30	25	20
65R-5-0/2.5	Coarse-grained	85	300	170	11	100	60	4	50	25	70
	Fine-grained	80	60	55	17	40	30	3	20	13	100
65R-5-2.5/5	Fine-grained	73	120	80	24	50	40	3	35	20	100
	Medium-grained	72	150	115	23	100	70	5	50	35	95
65R-5-23/26	Coarse-grained	80	350	210	18	45	30	2	80	36	40
	Fine-grained	83	400	240	13	100	60	4	60	50	100
65R-5-72/76	Coarse-grained	83	230	195	14	100	85	3	50	45	70
65R-5-80/84	Coarse-grained	76	200	125	21	200	95	3	50	30	95
	Fine-grained	77	120	90	19	70	55	4	50	27	100
65R-5-87/91	Fine-grained	77	125	100	20	75	63	3	30	26	100
65R-5-96/99	Fine-grained	78	80	80	17	50	40	5	40	35	100
	Coarse-grained	73	200	120	23	100	85	4	70	35	90

[a] Fine-grained (0.2–1 mm), coarse-grained (5–30 mm).
[b] Partly exsolved to troilite as identified with ore microscopy and EPMA.
[c] Average sulfide modes were calculated by dividing the cumulative area of given sulfide phase by the total area of all sulfide phases in a studied thin-section.
[d] Represents the five largest sulfide grains in given thin-section.
[e] Sulfide modes obtained using scanning electron microscopy and mineral liberation analysis. For other samples, we calculated sulfide modes using single sulfide images (see Section 3.2).

Table 2
Average major element contents (wt%) and elemental molar ratios of pyrrhotites (Po), troilites (Tro), chalcopyrites (Ccp), and pentlandites (Pn) from the upper igneous layering intervals (109.5–110.8 and 158.0–158.3 mbsf) of IODP Hole U1473A, Atlantis Bank, as determined by an electron microprobe.

Sample No.	Mineral	n[a]	Fe	Co	Ni	Cu	S	Total	Me/S ratio[b]	Co/Ni	Ni/(Ni + Fe)[c]	Cu/(Cu + Fe)[c]
13R-1-26-33	Po	17	59.4	0.1	0.5	0.1	38.2	98.3	0.90			
layer boundary	Ccp	16	30.1	<0.1	<0.1	34.6	34.5	99.3	1.01			0.50
	Pn	8	28.9	11.7	25.0	0.1	33.4	99.2	1.10	0.47	0.46	
13R-1-40-50	Po	12	59.2	<0.1	0.7	<0.4	38.4	98.4	0.90			
coarse-grained	Ccp	10	30.0	<0.1	<0.1	34.2	34.5	98.7	1.00			0.50
	Pn	5	30.2	6.7	28.7	<0.6	33.3	98.9	1.10	0.24	0.47	
13R-1-67-75A	Po	17	59.3	<0.1	0.6	0.1	38.4	98.5	0.90			
layer boundary	Ccp	16	29.9	<0.1	<0.1	34.6	34.8	99.3	1.00			0.50
	Pn	5	27.4	8.9	29.1	0.2	33.3	98.9	1.10	0.31	0.50	
13R-1-67-75B	Po	12	59.7	<0.1	0.6	<0.3	38.3	98.7	0.90			
layer boundary	Ccp	14	30.2	<0.1	<0.1	34.6	34.7	99.6	1.00			0.50
	Pn	2	26.7	11.4	28.1	<0.4	32.8	99.1	1.10	0.41	0.50	
13R-1-75-83	Po	9	60.2	<0.1	0.6	0.1	38.2	99.1	0.91			
fine-grained	Tro	6	61.8	<0.1	0.4	0.1	37.0	99.2	0.97			
	Ccp	8	30.5	<0.1	<0.1	34.8	34.6	99.9	1.02			0.50
	Pn	1	35.0	5.8	24.0	<0.4	34.2	99.0	1.06	0.24	0.40	
18R-1-18-25	Po	12	59.8	<0.1	0.4	0.1	37.8	98.1	0.92			
layer boundary	Tro	2	62.3	<0.1	<0.1	<0.3	36.4	98.7	0.98			
	Ccp	10	30.2	<0.1	<0.1	34.9	34.3	99.3	1.02			0.50
	Pn	8	28.7	8.8	27.7	0.4	33.0	98.6	1.11	0.32	0.48	

[a] n – number of measurements in given sample.
[b] Metal/S molar ratio.
[c] Molar ratio.

Table 3
Chemical composition of gabbros from igneous layering intervals (109.5–110.8 and 158.0–158.3 mbsf) of IODP Hole U1473A, Atlantis Bank.

Sample No.		13R-1-26/33	13R-1-40/50	13R-1-67/75	13R-1-75/83	18R-1-18/25
Grain size		Layer boundary[a]	Coarse	Layer boundary	Fine	Layer boundary
Depth (mbsf)		109.8	109.9	110.2	110.3	158.2
Major element contents (wt%)						
SiO_2	0.1[b]	50.47	50.24	51.14	50.35	50.9
TiO_2	0.001	0.50	0.56	0.65	0.55	0.45
Al_2O_3	0.05	16.44	16.05	14.2	15.69	15.53
Fe_2O_3	0.01	8.76	9.44	7.90	8.30	8.22
MnO	0.001	0.16	0.17	0.16	0.15	0.16
MgO	0.01	8.74	8.70	8.85	9.17	8.95
CaO	0.005	11.38	11.47	13.84	12.42	12.49
Na_2O	0.01	3.15	3.02	2.69	2.77	2.81
K_2O	0.005	0.06	0.06	0.04	0.04	0.05
P_2O_5	0.001	0.04	0.11	0.02	0.06	0.01
LOI	0.01	0.14	0.06	0.34	0.34	0.25
Total		99.82	99.88	99.83	99.83	99.81
Mg-number		66	65	69	69	68
Whole-rock chalcophile element contents (ppm)						
S	0.2[c]	1055	494	884	697	806
Cu	0.2	361	71.5	170	119	197
As	0.5	<0.5	<0.5	<0.5	<0.5	0.6
Zn	0.5	62.1	67.3	52.9	47.8	51.4
Ga	0.1	13.5	13.8	13.4	12.7	13.1
Pb	0.5	22.3	1.5	2.8	2.7	10.6
Sb	0.1	16.7	1.1	1.9	11.2	7.7
Ni	0.5	72.9	67.9	68.3	72.5	73.7
Ag	0.05	0.22	<0.05	<0.05	<0.05	0.09
Bi	0.02	0.02	<0.02	<0.02	<0.02	0.02
Cd	0.1	0.2	0.1	0.1	0.1	0.1

Table 3 (*Continued*)

Sample No.		65R-5-0/3*	65R-5-3/5*	65R-5-5/9	65R-5-14/22	65R-5-20/27*	65R-5-26-30	65R-5-48/56	65R-5-80/87*	65R-5-89/93	65R-5-95/101*	65R-5-99/104
Grain size		Layer boundary	Layer boundary	Layer boundary	Coarse	Layer boundary	Fine	Coarse	Layer boundary	Fine	Layer boundary	Coarse
Depth (mbsf)		593.0	593.0	593.1	593.2	593.3	593.3	593.5	593.8	593.9	594.0	594.0
Major element contents (wt%)												
SiO_2	0.05[b]	n/a	n/a	50.03	49.94	n/a	50.35	49.42	n/a	50.17	n/a	50.38
TiO_2	0.02			0.29	0.38		0.27	0.35		0.22		0.30
Al_2O_3	0.04			16.70	15.88		17.43	16.01		17.81		17.42
Fe_2O_3	0.015			5.70	6.34		5.23	6.65		4.68		5.96
MnO	0.015			0.11	0.12		0.10	0.12		0.09		0.11
MgO	0.03			10.20	10.81		9.44	10.83		9.08		10.03
CaO	0.03			13.21	13.22		13.38	12.66		13.67		12.85
Na_2O	0.02			2.59	2.47		2.74	2.52		2.74		2.72
K_2O	0.03			<0.03	<0.03		<0.03	<0.03		<0.03		<0.03
P_2O_5	0.1			<0.1	<0.1		<0.1	<0.1		<0.1		<0.1
LOI				0.41	0.10		0.17	0.08		0.22		n/a
Total				99.23	99.26		99.11	98.65		98.69		99.73
Mg-number				78	77		78	76		79		77
Whole-rock chalcophile element contents (ppm)												
S[c]		445	464	n/a	n/a	446	n/a	326[d]	n/a	344	371	n/a
Cu	2[b]	118	102	110	55	79	85	68	100	86	91	53
As	0.5	<0.5	<0.5	<0.5	<0.5	<0.5	<0.5	<0.5	<0.5	<0.5	<0.5	<0.5
Zn	7	112	34.3	25	29	20	23	31	23	20	20	27
Ga	0.02	14.2	12.6	12	12	14	13	12	13	13	12	13
Pb	0.5	567	68.7	69	<0.5	< 0.5	<0.5	<0.5	34	<0.5	<0.5	<0.5
Sb	0.06	8.8	1.9	1.9	<0.06	< 0.1	<0.06	<0.06	0.2	<0.06	<0.1	<0.06
Ni	2	90.3	139	133	126	112	112	134	115	114	125	119
Ag	0.05	1.0	0.1	n/d	n/a	<0.05	n/a	n/a	0.1	n/a	<0.05	n/a
Bi	0.05	0.2	0.04	0.04	<0.05	<0.02	<0.05	<0.05	0.0	<0.05	<0.02	<0.05
Cd	0.02	0.4	0.1	0.1	0.1	<0.1	0.07	0.1	<0.1	0.1	<0.1	0.1

mbsf – meters below seafloor; Fe_2O_3 = Total Fe as Fe_2O_3. LOI – loss-on-ignition; Mg-number = [molar Mg/(molar Mg + molar Fe)] × 100; n/a – not data available.

[a] Layer boundary zones represent the contact between the fine-and the coarse-grained gabbro (see Fig. 3).

[b] Detection limits.

[c] S content estimated according to petrographic description.

[d] S content estimated based on petrographic description of thin-section 65R-5-72/76 which showed the same lithology and grain size as 65R-5-48/56.

[*] Layer boundary samples that have been measured at Activation Laboratories Ltd. in Canada.

uncertainty was estimated as 1–6 relative percent. Loss-on-ignition (LOI) was used to determine the total volatile concentrations. For this purpose, samples were heated for 10 min in a muffle furnace at 1030 °C, having allowed volatiles to evaporate.

Chalcophile element concentrations for the upper intervals were determined via Instrumental Neutron Activation Analysis (INAA) and Inductively Coupled Plasma Mass Spectrometry (ICPMS) at the Activation Laboratories Ltd., Ontario, Canada with the Ultratrace 5 analytical package. The ICPMS measurements were conducted using a Perkin-Elmer Sciex ELAN 6000 spectrometer. The detailed analytical procedure, including standards and measurement conditions, is described in the Ultratrace 5 – Total Digestion – ICPMS, INAA subsection of the Methods section of the Actlab website (www.actlabs.com). Detection limits, accuracies, and precisions are shown in Table S3. Total S concentrations were determined at the Institut für Geologie und Paläontologie, University of Münster, Germany using an ELTRA CS800 carbon–sulfur analyzer. Approximately 75–100 mg of sample powder were placed in a porcelain crucible and combusted in an oxygen atmosphere at 1350 °C, and analyzed via infrared spectroscopy (see Lissner et al., 2014 for more details). Detection limit of the method was ~6 ppm S (Ciazela et al., 2018). We achieved accuracy of 7.3% (double relative standard deviation; 2RSD) based on two reference materials with 1.41% and 0.85% S. Six sample replicates indicate a precision of 2.1% (2RSD).

The major element oxide contents for the lower interval (Section 65R-5) were measured by Inductively Coupled Plasma-Optical Emission Spectrometry (ICP-OES) using an iCap6500 (Thermo Fisher Scientific, Waltham, USA), following the method of Govindaraju and Mevelle (1987) at the Service d'Analyse des Roches et des Minéraux (SARM) in Nancy, France. To monitor the uncertainty of the measurements, the diorite (DR-N) provided by SARM was measured as the reference material. Trace element contents for the lower interval were measured using the same instrument following the method of Carignan et al. (2001). Analytical accuracy and reproducibility were controlled by repeated analyses of five geochemical reference standards (for more details see Carignan et al., 2001). The related uncertainties, both for major and trace element contents, are presented in Tables S1 and S3. The whole-rock S contents (Table 3) were only estimated using sulfide contents and average S content of the sulfides (36 wt%; Table 1). We took into account the average densities of sulfide and silicate grains when sulfide contents expressed in vol.% were converted into wt%.

3.4. Whole-rock S isotopes

Sulfur extraction and S isotopic analyses were carried out at the Institut für Geologie und Paläontologie, University of Münster, Germany. Sulfide-S was extracted to Ag_2S as acid volatile sulfides (AVS) and Cr-reducible sulfur (CRS) using a modified method of Canfield et al. (1986). Acid volatile sulfides are related to monosulfides, including pyrrhotite ($Fe_{1-x}S$), troilite (FeS), and pentlandite ([Ni,Fe, Co]$_9S_8$), while Cr-reducible sulfur is associated with disulfides, such as chalcopyrite ($CuFeS_2$) (Oeser et al., 2012). Extraction was performed in a closed, all-glass digestion vessel, using 6 M HCl and a 1 M $CrCl_2$-HCl solution, respectively. All reactions were conducted in a nitrogen atmosphere (Canfield et al., 1986; Rice et al., 1993). The $^{34}S/^{32}S$ was measured using a Thermo Finningan Delta Plus MS. The results are reported in the standard delta notation ($\delta^{34}S$) as per mil differences to the Vienna Canyon Diablo Troilite (V-CDT) standard. Analytical performance was monitored using the IAEA –S1, –S2, –S3, and NBS 127 reference materials. Relative uncertainty for $\delta^{34}S$ values was within ±0.2‰ (2 standard deviations).

3.5. Scanning electron microscopy (SEM) and mineral liberation analysis (MLA)

We determined mapped minerals and quantified their modes in four selected thin sections (Figs. 3 and S2–S4; Tables 1 and S4) using a Quanta 650 FEG (FEI/Thermo Fisher Scientific, the Netherlands) SEM combined with MLA software version 3.0. The SEM was equipped with two Brucker energy-dispersive X-ray (EDX) detectors (XFlash Detector 5030, Silicon Drift Detector; Bruker Nano) for semi-quantitative element analysis without standardization and coupled to extended backscattered electron (XBSE) imaging (Fandrich et al., 2007). Initially, BSE images were collected using an acceleration voltage of 25 kV and a magnification of 500. Based on the grey values of the different minerals in the images, an automated function performed de-agglomeration and definition of individual minerals. The EDX analyses were performed using point mode with a spot size of 5 µm for every defined mineral. The measured mineral spectra were compared with the spectra of pre-defined mineral standards from the BGR database.

3.6. Electron microprobe analysis

The major element composition of sulfides (Tables 2 and S5) were determined using a Cameca SX 100 Electron Probe Microanalyzer (EPMA) at the Institute of Mineralogy, Leibniz University of Hannover, Germany. Standard materials for sulfides include native metals (Cu, Co), pyrite (S and Fe), and synthetic NiO. A current of 15 nA and an acceleration voltage of 15 kV were applied and results were corrected using the standard "PAP" algorithm (Pouchou and Pichoir, 1991). The detection limits, accuracy, and precision of the EPMA measurements are shown in Table S6.

3.7. Laser ablation – Inductively coupled plasma mass spectrometry

3.7.1. Trace elements analysis

To determine chalcophile and Platinum Group Element (PGE) concentrations (Tables S7–S9), we used an ELEMENT-XR (Thermo Fisher Scientific, Germany) fast-scanning sector field ICPMS coupled to a femtosecond laser ablation (fs-LA) system (Solstice, Spectra-Physics, USA) at the Institute of Mineralogy, Leibniz University of Han-

nover, Germany. The laser unit operates in the deep UV at 194 nm and produces energy pulses of 50 mJ in the fourth harmonic. The ultrashort pulses prevent elemental fractionation at the sample site and to minimize matrix effects (Horn and von Blanckenburg, 2007). During tuning, low ThO/Th was set (≤0.4%) to limit the rate of oxide formation. At the start and end of each session, the NIST610 and PGE-A reference materials were measured as external standards. We used laser beam diameters of 60 μm for the standards and of 10–60 μm for sulfide grains. The repetition rate was 10 Hz for the standards and 42–71 Hz for the sulfides. Ablated particles were removed from the sample chamber using a He carrier gas mixed with Ar before entering the ICPMS. We used the Fe, Ni, and Cu contents measured with EPMA as internal standards. Data were reduced using the Matlab-based SILLS software (Guillong et al., 2008), including drift correction. Furthermore, the light PGEs (that is ^{99}Ru, ^{101}Ru, ^{103}Rh, ^{105}Pd, and ^{106}Pd) isotopes required interference correction for the argides of ^{59}Co, ^{61}Ni, ^{63}Cu, ^{65}Cu, and ^{66}Zn. The interferences were corrected by measuring the Co-rich pyrite (MAC), native Ni, native Cu, as well as ZnS (MAC) reference materials and comparing the pure metal signals to the metal argide signals. The detection limits and sample errors for the LA-ICPMS measurements are presented in Table S10.

3.7.2. Copper isotope analysis

The Cu isotopic composition of chalcopyrite was determined using the same fs-LA system combined with a NeptunePlus (Thermo Fisher Scientific, Germany) multi-collector (MC) ICPMS at the Institute of Mineralogy, Leibniz University of Hannover, Germany. The ICPMS was operated in low resolution mode. The ^{62}Ni/^{60}Ni ratio was measured along with the Cu isotopes to correct for mass bias. For this study, diluted NIST SRM 986 standard solution with 0.5 ppm Ni was introduced using a quartz glass spray chamber (double pass Scott design) and a PFA micro-flow nebulizer with an uptake rate of ~100 μL/min.

The Cu isotopes of chalcopyrites were measured against the Cu NIST SRM 976 standard and reported as δ^{65}Cu (i.e., deviation of ^{65}Cu/^{63}Cu from NIST SRM 976 expressed in ‰). In addition, the Cpy1 standard from Lazarov and Horn (2015) was measured to verify that the laser performed with appropriate energy and δ^{65}Cu we obtained agree with δ^{65}Cu obtained by Lazarov and Horn (2015; 0.18–0.37‰). All samples and both standards were ablated along lines with a laser beam of 40 μm and repetition rates of 2.5–2.9 Hz for the NIST SRM 976 and 7.1–7.7 Hz for the Cpy1. We achieved relative standard errors (RSE) of <0.1% calculated by propagation of the within-run RSE of a sample and its two bracketing standards (Table S11).

3.7.3. Iron isotope analysis

The Fe isotopes of eight pyrrhotites, one pentlandite, and thirteen chalcopyrites were measured using the same fs-LA-MC-ICPMS against the IRMM-014 standard and reported as δ^{56}Fe and δ^{57}Fe (i.e., deviations of ^{56}Fe/^{54}Fe and ^{57}Fe/^{54}Fe relative to the IRMM-014 standard expressed in ‰). In addition, an in-house JM puratronic (PURA) Fe-standard (99.995% Puratronic, Johnson Matthey, lot No. FE495007IF2) was measured (see Tables S12 and S13) at the beginning of each analytical session to verify that the laser has an appropriate energy and the obtained δ^{56}Fe agree with those reported by Horn et al. (2006). All the sulfides and both the standards were ablated along 50-μm-wide (pentlandite) or 60-μm-wide lines. We achieved RSEs of <0.2‰ (see Table S12).

3.8. SHRIMP measurements

In addition to bulk-rock material, ^{32}S and ^{34}S were measured in pyrrhotites and chalcopyrites by Sensitive High-Resolution Ion Microprobe (SHRIMP Ile/MC) at the Micro-area Analysis Laboratory Ion Microprobe Facility, Polish Geological Institute-National Research Institute (PGI-NRI), Warsaw, Poland. Rock subsamples containing the largest sulfide grains, along with the standards (the Cpy1 and Cpy2 chalcopyrites and the Sudbury pyrrhotite; Fiege et al., 2014; Li et al., 2020 and references therein), were embedded in epoxy resin, polished, and coated with gold. The S isotopic composition of the chalcopyrite standards were previously measured using secondary ion mass spectrometry by two independent laboratories (Centre for Ore Deposit and Earth Sciences at the University of Tasmania and Geochronology Laboratories, Chelmsford, MA), and the δ^{34}S reference values are +1.4 ± 0.2‰ (1σ) for the Cpy1 standard and −0.7 ± 0.5‰ (1σ) for the Cpy2 standard, respectively. The Sudbury pyrrhotite shows a δ^{34}S reference value of +2.4 ± 0.2‰ (1σ) measured in solution using the Kiba extraction method (Ripley et al., 2011). The spots for analyses were selected using an optical microscope and BSE images using a SU3500 SEM (Hitachi, Tokyo, Japan) (Fig. S6). Analyzed sulfides (chalcopyrite and pyrrhotite) were bombarded with a high energy primary beam of Cs^+ ions in a high vacuum with a spot diameter of 26 μm and a depth of <5 μm. For the chalcopyrites, we used a 4 nA primary beam with an accelerating voltage of 15 kV, a mass resolution (M/ΔM) of 2000, and Faraday cups. For the pyrrhotite, we changed the current of the primary beam to 5 nA. The standards were measured every three spots. Data were reduced using the POXY software and are presented in Table S14.

4. RESULTS

4.1. Petrographic characteristics

Most samples are olivine gabbros (>5% modal olivine), with only 13R-1-26/33, 18R-1-18/25, and 65R-5-2.5/5 classified as gabbro (<5% modal olivine) (Table S4). Sulfides formed irregular or globular grains, from tens to hundreds of micrometers in size (Fig. 4A–D). The sulfides were mostly interstitial, located at the rims of olivines and clinopyroxenes (Fig. 4G and H), and were associated with Fe-Ti oxides, brown amphibole (Fig. 4E and F), and apatite (Fig. S2). Some of these sulfides formed inclusions within or intergrowths with the oxides (Fig. 4B). The oxides were titanomagnetites and exsolutions of titanomagnetite with ilmenite (Fig. 4B). In addition, we observed small sulfides

enclosed in clinopyroxene or plagioclase, mostly oriented along cleavage planes.

Petrographic description indicates sulfide enrichment along the boundaries between the coarse- and fine-grained gabbros, both in the upper (109.5–110.8 and 158.0–158.3 mbsf), and the lower (593.0–594.0 mbsf), intervals. The boundaries from the upper interval (Sections 13R-1 and 18R-1) exhibited higher sulfide contents (~0.15 vol.%) than the other samples (~0.10 vol.% for fine- and ~0.08 vol.% for coarse-grained gabbro; Fig. 2), as revealed by the SEM MLA analysis (Figs. 2 and S2–S4). Similarly, in the lower interval, the thin-sections containing layer boundary exhibited higher sulfide contents of sulfide grains (~0.074 vol.%) compared to the coarse- (~0.059 vol.%) and fine-grained (~0.062 vol.%) samples (Fig. 2).

The sulfides formed polymineral grains except for rare monophase pyrrhotite or chalcopyrite grains. On average, sulfide grains were composed of 81 vol.% pyrrhotite [$Fe_{1-x}S$], 16 vol.% chalcopyrite [$CuFeS_2$], and 3 vol.% pentlandite [$(Ni,Fe)_9S_8$] (see Table 1). The pyrrhotite ranged between 60 and 1000 μm (typically ~200 μm), and contained troilite exsolutions, observed in microscopic and BSE images (Fig. 4D), and confirmed with the EPMA measurements (Tables 2 and S5). The pentlandite was mostly dispersed throughout the pyrrhotite forming the smallest crystals with typical size of ~30 μm showing exsolution textures between pentlandite and pyrrhotite. In contrast, chalcopyrite formed mostly massive crystals, with an average size of 70 μm, in most cases on the rims of the sulfide grains (Fig. 4A–C).

Compared to the lower interval (593.0–594.0 mbsf), the sulfide grains from the upper intervals (109.5–110.8 and 158.0–158.3 mbsf) were larger (Table 1) and relatively rich in pyrrhotite (84 vol.%), but poor in chalcopyrite (14 vol.%) and pentlandite (2 vol.%). Sulfides of the lower interval contained only 77 vol.% of pyrrhotite but were rich in chalcopyrite (19 vol.%) and pentlandite (4 vol.%). The size of sulfide grains also differed between domains, with up to 1000 μm in the coarse-grained gabbro, and to 370 μm in the fine-grained gabbro (Table 1).

4.2. Whole-rock composition

The igneous evolution of different groups of samples is well expressed by whole-rock Mg-numbers. The upper intervals (Sections 13R-1 and 18R-1) exhibited Mg-numbers between 65 and 69, whereas the lower interval (65R-5) showed Mg-numbers of 76–79 (Table 3). All the intervals showed low SiO_2 contents (49.4–51.1 wt%; Table 3). In addition, the coarse-grained samples showed lower Mg-numbers (65 and 77 for Units II and VII, respec-

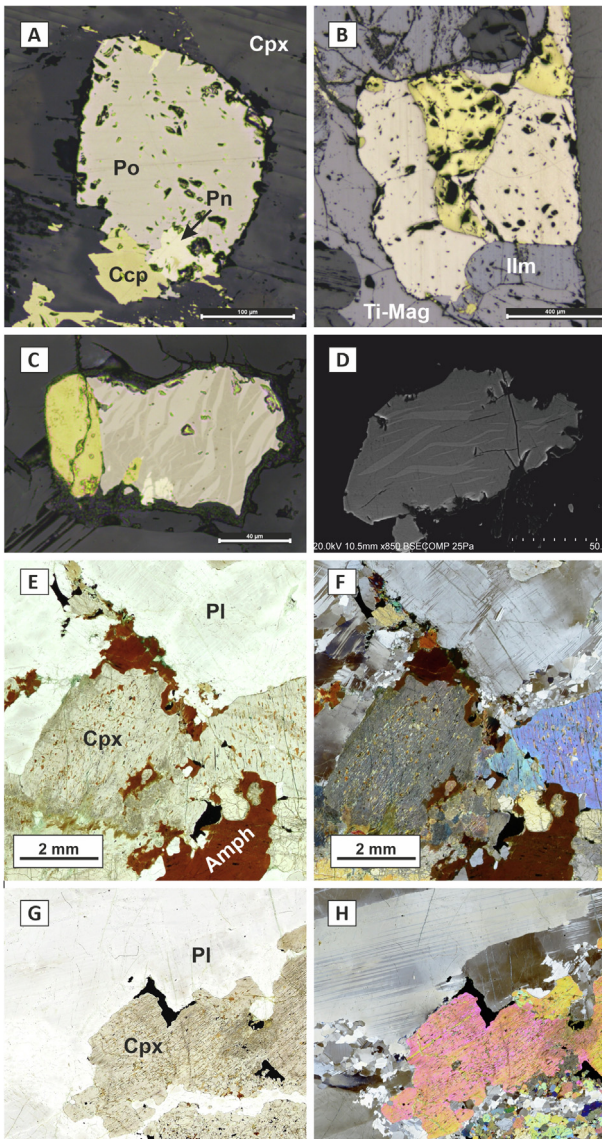

Fig. 4. (A) Globular sulfide (yellow) enclosed in clinopyroxene (dark grey with the cleavage). The exsolutions of pentlandite (Pn) in pyrrhotite (Po) formed after monosulfide solid solution, whereas chalcopyrite (Ccp) forms massive crystals on the rims of the sulfide grain. Sample U1473A-13R-1 40/50-CIAZ. Reflected light. (B) Irregular sulfide grains associated with ilmenite (Ilm) and titanomagnetite (Ti-Mag). Sample U1473A-13R-1 67/75A-CIAZ. Reflected light. (C) Sulfide grain with distinct troilite (dark brown bands) exsolved from pyrrhotite (light brown bands) in Sample U1473A-65R-5 72/76. Reflected light. (D) Troilite (light grey bands) exsolved from pyrrhotite (dark grey bands) in Sample U1473A-18R-1-18/25-CIAZ. Back-scattered electron (BSE) image. (E) Sulfide grains (black) at the rim of clinopyroxenes and plagioclases that are associated with the brown amphiboles. Sample U1473A-13R-1 40/50-CIAZ. Transmitted light. (F) Corresponding image under cross-polarized light. Note, that at the boundaries of coarse-grained silicates we can observe a thin zone of fine-grained rock within which the sulfides were crystalized. (G) Interstitial oxides (ilmenite and Ti-magnetite) and sulfide grains (black) at the rim of clinopyroxenes. Sample U1473A-13R-1 26/33-CIAZ. Transmitted light. (H) Corresponding image under cross-polarized light. A small-scale example that sulfides most likely precipitated at the boundary between coarse- and fine-grained zones. (G) and (H) images corelate with scanning electron microscopy mineral liberation analysis showing the mineral distribution of Fig. 2.

tively) compared to the fine-grained gabbroic rocks with Mg-numbers of 69 in Unit II and 79 in Unit VII, respectively. The boundaries displayed intermediate Mg-numbers (66–69 and 78, respectively) (Tables 3 and S4). These observations are further supported by the rare earth elements (REE) patterns, with generally higher REE contents in the upper interval, and coarse-grained samples (Fig. S7). Major element contents of gabbroic rocks from the studied igneous layering intervals were relatively homogenous, with standard deviations of mostly <1.0 wt % (Table 3). The analyzed rocks were fresh, or only minimally altered, as confirmed by their low average LOI of 0.21 wt% (Table 3).

We observed a correlation between the sulfide contents and the chalcophile element contents. In the studied intervals (Cores 13R-1, 18R-1, and 65R-5), the boundaries between fine- and coarse-grained gabbros generally exhibited higher contents of chalcophile elements, in agreement with the higher sulfide contents observed at those boundaries. For mass balance calculations, we assumed the average thickness of the layer boundaries was 5.7 ± 2.1 cm (1SD; n = 9) based on the average thickness of the measured layer boundary samples. The boundary samples from the upper intervals contained, on average more S (915 ± 103 ppm; 1SD), than the coarse-grained (494 ppm S) and fine-grained (697 ppm S) gabbros (Table 3 and Fig. 2). The average S content for Unit II was 386 ppm (MacLeod et al., 2017). The boundaries had higher Cu (on average 243 ± 84 ppm Cu; 1SD) and Pb (12 ± 0.8 ppm; 1SD) concentrations relative to the coarse-grained (72 ppm Cu and 1.5 ppm Pb) and fine-grained (119 ppm Cu and 2.7 ppm Pb) gabbro (Table 3).

The ~6 cm-thick boundaries between the fine- and coarse-grained gabbros from the lower interval also revealed higher Cu concentrations (on average 100 ± 13 ppm; 1SD) relative to the fine-grained (86 ± 1 ppm Cu; 1SD) and coarse-grained gabbros (58 ± 7 ppm Cu; 1SD) (Fig. 2). Based on the petrographic description, we estimated the S content for the lower interval samples (see Section 3.2). The boundaries were generally enriched in S (432 ± 36 ppm S; 1SD) and Pb (185 ± 255 ppm; 1SD), compared to fine- (344 ppm S), and coarse-grained domains (326 ppm S). Lead contents for fine- and coarse-grained gabbros from Unit VII were below the limit of detection (0.5 ppm). The Cu and S contents exhibited positive correlations for the studied intervals (Fig. S8). The average concentrations for Units II and VII were 52 ± 42 ppm Cu and 386 ± 462 ppm S (1SD), as well as 66 ± 49 ppm Cu and 408 ± 195 ppm S (1SD), respectively (MacLeod et al., 2017). The average Pb content (2.5 ± 4.1 ppm; 1SD) reported is based on our post-cruise measurements (Table S15).

4.3. Major element compositions of sulfides

We analyzed the major element compositions of pyrrhotite, chalcopyrite, and pentlandite in the six samples from the two upper intervals (one sample was duplicated; Table 2 and Table S5). The pyrrhotite is characterized by nearly constant Fe (59.2–60.2 wt%), and low Ni contents (up to 0.7 wt%). The metal/S ratio ranges from 0.90 to 0.92, in agreement with the stoichiometric formula of the hexagonal pyrrhotite ($Fe_{11}S_{12}$) (Vaughan and Corkhill, 2017). However, there are also troilite exsolutions within pyrrhotite with a metal/S ratio of 0.98. Chalcopyrite is on average composed of 30.1 wt% Fe, 34.7 wt% Cu, and 34.6 wt% S, consistently showing stoichiometric Cu/(Cu + Fe) ratios of 0.50. Pentlandite has a metal/S ratio of 1.11 ± 0.02 (1SD), close to the stoichiometric formula of Me_9S_8, except for one sample 13R-1-75-83 with a ratio of 1.06. The Co content of pentlandite range between 5.8–11.7 wt% (Fig. 2). Interestingly, the pentlandites occurring at the boundary between the fine- and coarse-grained gabbros are Co-rich (10.2 ± 1.4 wt%, 1SD), whereas they are Co-poor elsewhere (6.3 ± 0.6 wt%, 1SD; Tables 2 and S5). The Ni/(Ni + Fe) ratio of pentlandites is ~0.50, except for Sample 13R-1-75/83, with 0.40.

4.4. Trace element composition of sulfides

Cobalt, Ni, Cu, Zn, Ga, Ge, As, Se, Ag, Cd, In, Sn, Re, Au, Tl, Pb, Bi and PGEs including Os, Ir, Ru, Rh, Pt, and Pd were measured in pyrrhotite, chalcopyrite and pentlandite (Table S7–S9 and Fig. S9).

Pyrrhotite exhibited relatively homogenous trace element compositions. Copper concentrations ranged from 25 to 132 ppm. Zinc and Se were present but always <50 ppm. Thallium is a trace element characteristic of MORB-derived pyrrhotite (e.g., Ciazela et al., 2018) and was detected in all our samples, with concentrations to 0.55 ppm. PGEs were detected in most pyrrhotite grains (Table S7), and were especially rich in Os and Ir, compared to the pentlandite and chalcopyrite.

Fifteen chalcopyrite crystals were measured for trace element compositions (Table S8). Cobalt and Ni occurred in trace amounts, at 21–51 ppm and 111–455 ppm, respectively. One small chalcopyrite measured in the fine-grained gabbro (thin section 13R-1-75/83) contained anomalous Co (1469 ppm) and Ni (6871 ppm) contents for chalcopyrite, indicating contamination from neighboring pentlandite. Zinc (3237 ppm), Ag (21 ppm), Cd (15 ppm), Ru (3.6 ppm) and Rh (35 ppm) contents in this chalcopyrite were much higher than averages for pentlandites and thus any contamination would be negligible for these elements. Zn was high in chalcopyrites (904–3237 ppm), as were Ag (4–21 ppm) and Pb (2.1–8.4 ppm). PGEs behave according to their physical and chemical behavior (e.g., density and fusion temperature; Mondal, 2011), and are divided into two subgroups: Ir-PGE (i.e., Ir, Os, Ru) and Pd-PGE (i.e., Pd, Pt, Rh) (Barnes et al., 1985). Pd-PGEs show affinity to chalcopyrite and were detected in most samples. Note that chalcopyrites from the boundary zones and fine-grained gabbros were heavily enriched in Rh and Pd with respect to those from the coarse-grained gabbros (Fig. 6). Osmium (1 ppb) and Ir (3 ppb) were detected only in the boundary samples.

In most pentlandites, trace elements were below the detection limits due to the small size of the grains

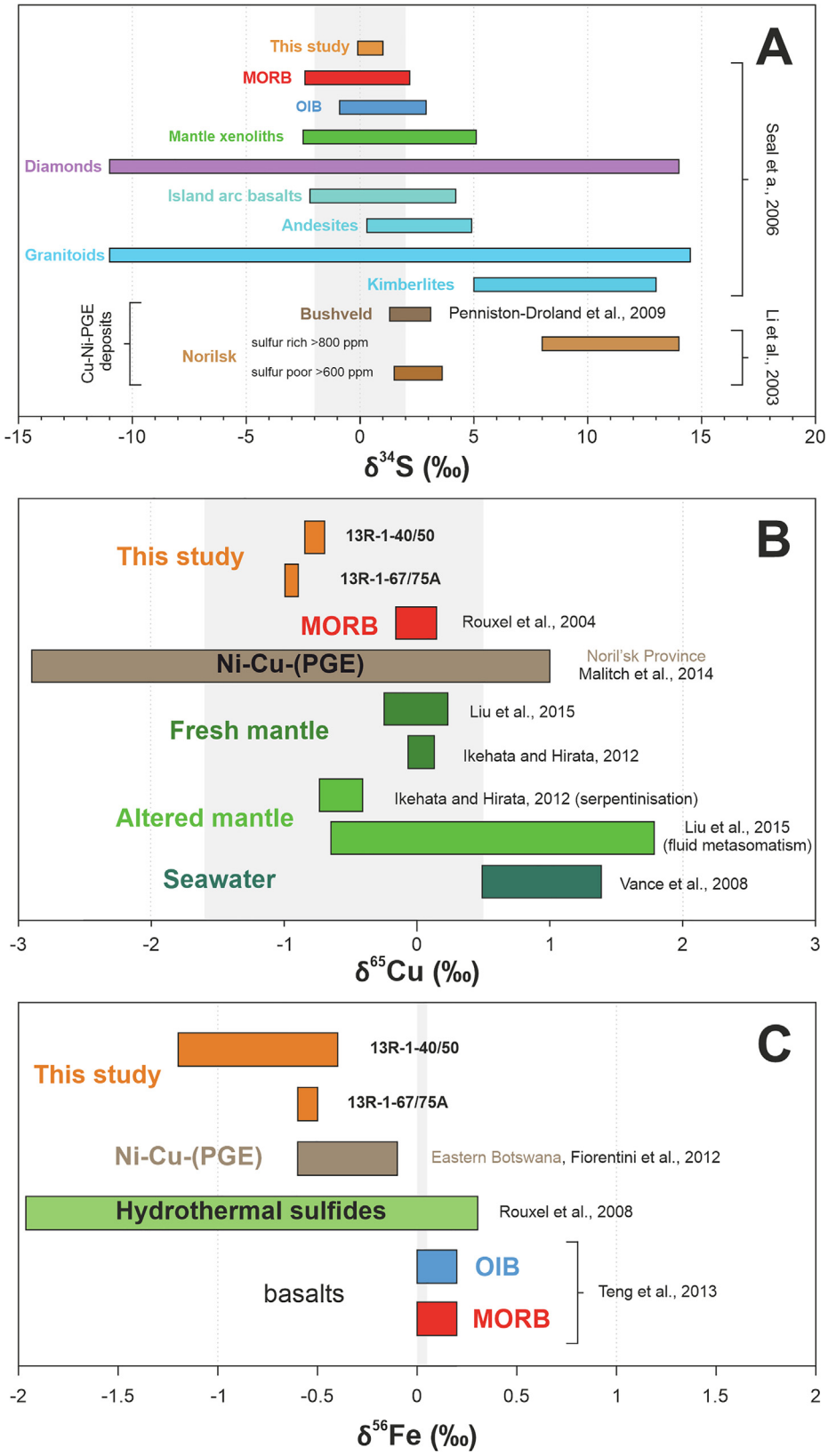
A
This study
MORB
OIB
Mantle xenoliths
Diamonds
Island arc basalts
Andesites
Granitoids
Kimberlites
Seal et a., 2006
Cu-Ni-PGE deposits
Bushveld
Penniston-Droland et al., 2009
Norilsk
sulfur rich >800 ppm
sulfur poor >600 ppm
Li et al., 2003
-15 -10 -5 0 5 10 15 20
δ34S (‰)
B
This study
13R-1-40/50
13R-1-67/75A
MORB
Rouxel et al., 2004
Ni-Cu-(PGE)
Noril'sk Province
Malitch et al., 2014
Fresh mantle
Liu et al., 2015
Ikehata and Hirata, 2012
Altered mantle
Ikehata and Hirata, 2012 (serpentinisation)
Liu et al., 2015
(fluid metasomatism)
Seawater
Vance et al., 2008
-3 -2 -1 0 1 2 3
δ65Cu (‰)
C
This study
13R-1-40/50
13R-1-67/75A
Ni-Cu-(PGE)
Eastern Botswana, Fiorentini et al., 2012
Hydrothermal sulfides
Rouxel et al., 2008
basalts
OIB
MORB
Teng et al., 2013
-2 -1.5 -1 -0.5 0 0.5 1 1.5 2
δ56Fe (‰)

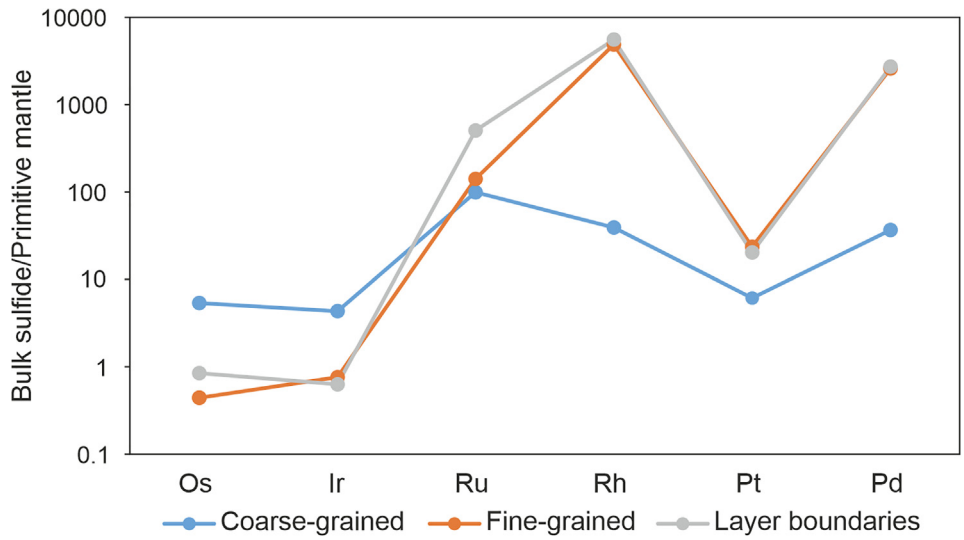

Fig. 6. Bulk-sulfide PGE contents normalized to primitive mantle for the coarse- and fine-grained gabbro, as well as the boundaries between them in IODP Hole U1473A. The primitive mantle contents are from McDonough and Sun (1995). Note that the sulfides documented in the coarse-grained gabbro are enriched in Ir-PGE (Os and Ir), whereas the sulfides from the fine-grained gabbros are enriched in Pd-PGE (Rh, Pt, and Pd). The sulfides from the boundary zones between the coarse-grained and fine-grained gabbros are also enriched in Pd-PGE and show a pattern similar to that of the fine-grained gabbro sulfides. This pattern is in contrast to the coarse-grained gabbro.

(typically < 30 μm; see Section 4.1). The average Cu content in pentlandites ranged from 731 ppm up to 32,417 ppm. Similarly, elevated Zn contents were found in most investigated pentlandites (up to 3209 ppm; Table S9). Only in two of our samples were Zn contents below 100 ppm. We think that chalcopyrite contamination from tiny crystals hidden under the surface of pentlandite affected the concentrations of Cu and Zn measured. This was not the case for Pb (18 ppm) and Bi (8.1 ppm), which were much higher in the pentlandites than the chalcopyrites and pyrrhotites (Table S9). Among PGEs, only Ru and Rh were present in all samples, whereas other PGEs, in most cases, were under detection limits due to the small size of pentlandite crystals. The Ru (1.3–4.3 ppm) and Rh (1.1–3.7 ppm) concentrations were relatively constant among the studied samples. Osmium was detected once (0.23 ppm in 13R-1-40/50), and Ir never exceeded the detection limits (<0.1 ppm).

4.5. Sulfur speciation and isotope composition

Sulfur present in the upper igneous layering interval was generally bound as sulfide-S (Table 4), either as AVS or CRS, with CRS always prevailing (Table 4, see Section 3.3). The S isotopes were determined both as total bulk sulfide-S, and separately, as AVS-S and CRS-S (Table 4). The sulfide-S $\delta^{34}S$ ranged from –0.1‰ to +1.0‰ throughout the entire igneous layering interval, with no systematic differences between various rock types (Table 4, Figs. 2 and 5a). Notably, the $\delta^{34}S$ in CRS-S was positive (+0.1 to +1.3‰) and consistently higher than AVS-S, which exhibited negative values (–0.6 to –0.1‰; Table 4). Consistently, our *in situ* SHRIMP measurements revealed that the $\delta^{34}S$ of pyrrhotite was consistently positive (+1.6‰ to + 1.7‰), in contrast to negative signatures in chalcopyrites (–2.1‰ to –1.7‰). The weighted average $\delta^{34}S$ for the measured bulk grains was +1.3‰ (Table S14).

4.6. Copper and iron isotopic composition

The Cu and Fe isotopes were measured in two samples, 13R-1-40/50 (coarse-grained gabbro) and 13R-1-67/75A (boundary). The $\delta^{65}Cu$ signatures of measured chalcopyrites were consistently low, ranging from –0.9‰ to –0.7‰ for the coarse-grained gabbro, and –1.0‰ to –0.9‰ for the boundary (Fig. 5B, Table S11). The $\delta^{56}Fe$ signatures

Fig. 5. (A) Comparison of the $\delta^{34}S$ signatures from this and other studies. The gray shaded band represents the S isotopic composition of the mantle considered to be 0 ± 2‰ (Seal, 2006). (B) The $\delta^{65}Cu$ (‰) signatures of chalcopyrites from the upper igneous layering intervals (109.5–110.8 and 158.0–158.3 mbsf) of IODP Hole U1473A measured using LA-ICPMS. Our results are compared to those from other geological settings. The gray shaded-band shows the $\delta^{65}Cu$ values for magmatic chalcopyrites (−1.6‰ to +0.4‰) (Zhu et al., 2000; Larson et al., 2003; Malitch et al., 2014). (C) The $\delta^{56}Fe$ (‰) signatures of our pyrrhotites in comparison with other studies related to Fe isotope in sulfides. The gray shaded band represents the average Fe isotopic composition ($\delta^{56}Fe$) of the terrestrial mantle $\delta^{56}Fe = +0.025 \pm 0.025$‰ (Craddock et al., 2013).

Table 4
Summary table of whole-rock S speciation and isotopic compositions of gabbros from the upper igneous layering intervals (109.5–110.8 and 158.0–158.3 mbsf) of IODP Hole U1473A, Atlantis Bank.

Sample No.	13R-1-26/33	13R-1-40/50	13R-1-67/75	13R-1-75/83	18R-1-18/25
Grain size	Layer boundary[a]	Coarse	Layer boundary	Fine	Layer boundary
Depth (mbsf)	109.8	109.9	110.2	110.3	158.2
S speciation and isotopic composition					
Sulfide-S (ppm)	1113	585	907	720	848
(AVS + CRS)/TS	1.05	1.18	1.03	1.03	1.05
AVS (ppm)	261	109	286	177	n/a
$\delta^{34}S_{AVS}$ (‰ V-CDT)	−0.1	−0.5	−0.5	−0.6	n/a
CRS (ppm)	852	476	621	543	n/a
$\delta^{34}S_{CRS}$ (‰ V-CDT)	1.3	0.3	0.1	0.6	n/a
$\delta^{34}S_{AVS+CRS}$ (‰ V-CDT)	1	0.2	−0.1	0.3	0.6

TS – total S; AVS – acid volatile sulfide; CRS – chromium reducible sulfur; n/a – not available.
[a] Layer boundary represent the contact between the fine-grained and coarse-grained gabbro (see Fig. 3).

of measured pyrrhotites were negative, ranging from –1.2‰ to –0.4‰ for the coarse-grained gabbro and from –0.6‰ to –0.5‰ for the boundary (Fig. 5C, Table S12). In contrast, the δ^{56}Fe signature of pentlandite revealed a positive value of +1.3‰ (coarse-grained; Table S12). Similar to pentlandite, the δ^{56}Fe signature of chalcopyrites from 615–730 mbsf interval revealed an average value of +1.44 ± 0.09 ‰ (1SD; Table S13).

5. DISCUSSION

5.1. Magmatic origin of sulfides

5.1.1. Texture and composition of the sulfides

The investigated sulfides are pyrrhotite-chalcopyrite-pentlandite-troilite assemblages (Section 4.1) interpreted as having crystallized from mafic magmas, known from the lower oceanic crust (Alt and Anderson, 1991; Miller and Cervantes, 2002) and igneous sulfide deposits including the Bushveld Complex (Ballhaus and Sylvester, 2000). Distinct minerals crystallize from the sulfide liquid upon cooling. Monosulfide solid solution (mss) crystallizes first from sulfide droplets at ~1000 °C. The mss is Ni-rich compared to residual Cu-rich liquid, which precipitates as intermediate solid solution (iss) at ~900 °C. Due to subsequent recrystallization of the mss and iss, pyrrhotite, pentlandite, and chalcopyrite form at temperatures <650 °C (Ballhaus and Sylvester, 2000; Holwell and McDonald, 2010). Finally, troilite exsolves from Fe-rich pyrrhotite (>48% atomic Fe) at <140 °C (Kissin and Scott, 1982).

Exsolutions of pentlandite in oriented lamellae (see Fig. 4A) indicate a slow cooling rate of ~1 °C/h (Francis et al., 1976; Durazzo and Taylor, 1982) consistent with the plutonic origin of the samples. Constraints on the temperature of pentlandite crystallization are provided by the major element composition of pentlandites (Fig. S10). In our study, pentlandites were Co-rich (>5 wt%; Tables 2 and S5), which combined with their typically low Fe content (<30 wt%), indicate a high-temperature formation. The higher range of Ni/(Ni + Fe) is more likely to occur in high-temperature sulfides (Kaneda et al., 1986), supporting our previous considerations that the sulfides formed at magmatic temperatures, and the pentlandite exsolved upon cooling. Comparison with experimental results from Kaneda et al. (1986) suggest that our pentlandite and pyrrhotite exsolved from mss at >400 °C (Fig. S10).

We have demonstrated that the sulfide grains were texturally associated with Fe-Ti oxides, brown amphiboles, and apatites (Section 4.1; Figs. 3 and 4). The coexistence of these typical late-stage magmatic minerals indicates percolation of melts during the late magmatic stage < 1050 °C (Natland et al., 1991; Natland and Dick, 2001; Koepke et al., 2018). After the main stage of MORB-like melt crystallization, late-stage melts might be squeezed into and accumulated in higher-permeability zones, resulting in the precipitation of late-stage minerals. Similar mineral associations have also been found in the oxide and olivine gabbros of Hole 735B by Natland et al. (1991)1 and Ozawa et al. (1991) and interpreted to have magmatic origin.

5.1.2. Isotope systems

Magmatic sulfides may form from S-rich mantle-derived melts or S-undersaturated magmas that assimilated altered country rocks enriched in seawater S (Barnes and Lightfoot, 2005). Addition of seawater-derived S (δ^{34}S = +21‰; Tostevin et al., 2014) would cause higher δ^{34}S values of such sulfides (from +2.0 to +8.8‰; Peters et al., 2010), in contrast to the mantle S, which is typically within 0 ± 2‰ (Ripley and Li, 2003; Seal, 2006; Alt et al., 2007; Oeser et al., 2012; Shanks, 2013). The δ^{34}S signatures of our whole-rock samples ranged from –0.1‰ to +1.0‰ (Section 4.5, Figs. 4 and 5A) suggesting a purely mantle origin for the parental melts. Those results are consistent with the mantle-like δ^{34}S signatures (an average of +0.2‰) of olivine-rich gabbroic rocks with sulfides that were reported in a similar geological setting at the Atlantis Massif OCC (MAR; IODP Hole U1309D; Delacour et al., 2008).

As mentioned in Section 4.5, pyrrhotites studied herein displayed average δ^{34}S values of 1.7‰, contrasting to chalcopyrites that displayed a δ^{34}S of –1.9‰ (Table S14 and Fig. S6). This results in a difference of 3.6‰. Calculations of S isotope fractionation in sulfides (Kajiwra and Krouse, 1971; Li and Liu, 2006) suggest that pyrrhotite should indeed display ^{34}S enriched values compared to

chalcopyrite. However, the predicted S isotope equilibrium fractionation between pyrrhotite and chalcopyrite ($\Delta^{34}S_{Po-Ccp}$) is only +0.4‰ at 650 °C (Li and Liu, 2006), in contrast to the large $\delta^{34}S$ difference in our samples. As the sulfides are of magmatic origin our results likely indicate that isotopic equilibrium was not maintained during cooling. The equilibrium might have been disturbed by kinetic fractionation effects likely related to S diffusion between the phases (Seal, 2006).

Further constraints on sulfide formation were obtained with the Cu isotopes. Similar to other isotope systems, copper isotope fractionation decreases with increasing temperature and is limited during magmatic differentiation (Larson et al., 2003). A mantle-derived $\delta^{65}Cu$ is considered to be near 0.0‰ in whole-rock measurements (Liu et al., 2015; Savage et al., 2015). However, such a whole-rock signature is a mixture of $\delta^{65}Cu$ for chalcopyrites and silicate minerals. For example, negative $\delta^{65}Cu$ for chalcopyrites and positive $\delta^{65}Cu$ for silicates may result in $\delta^{65}Cu$ of 0.0‰ as in magmatic bulk-rock samples. This seems to be the case for some chalcopyrites from mafic intrusions, where chalcopyrites show a total $\delta^{65}Cu$ variation of 2‰, ranging from –1.6‰ to +0.4‰ (Zhu et al., 2000; Larson et al., 2003; Malitch et al., 2014). In our study, the chalcopyrites exhibited $\delta^{65}Cu$ values between –1.0‰ and –0.7‰ (Fig. 5B and Table S11), in agreement with the aforementioned reports on magmatic sulfides. Our results, combined with the previous studies, indicate that segregation of magmatic sulfides from silicate melts is accompanied by negative Cu isotope fractionation.

The bulk-rock $\delta^{56}Fe$ of magmatic rocks, including gabbros, MORBs and fresh peridotites, show a narrow range of 0 ± 0.1‰ (Dauphas et al., 2009; Wu et al., 2018; Peters et al., 2019 and references therein). In contrast, the $\delta^{56}Fe$ of hydrothermal sulfides varies between –1.9‰ and –0.1‰ (Rouxel et al., 2008). In the present study, we measured *in situ* $\delta^{56}Fe$ of igneous sulfides that form polyphase grains (see Section 4.1). The pyrrhotites displayed negative values of $\delta^{56}Fe$, ranging from –0.38‰ to –1.20‰ (Fig. 5C). In contrast, the only measured pentlandite exhibited a positive value (+1.28‰; Table S13). Although we did not measure associated chalcopyrite, our measurements of 13 chalcopyrite grains in similar sulfides from a lower 615–730 mbsf interval yielded an average of +1.44 ± 0.09‰ (1SD; Table S13). Subsequently, we calculated the bulk sulfide $\delta^{56}Fe$ for one representative sulfide grain (Sa; Fig. 4A) in Sample 13R-1-40/50 (Tables S12–S13). This grain was composed of 80% pyrrhotite, with a $\delta^{56}Fe$ of –0.38‰, 8% pentlandite (+1.28‰), and 12% of chalcopyrite (the assumed average value of +1.44‰), which yields a bulk $\delta^{56}Fe$ of –0.03‰, calculated as a weighted average. This conforms with typical mantle-derived $\delta^{56}Fe$, further supporting a magmatic origin of the investigated sulfides. These results are also one of the first confirmations for a significant Fe isotopic fractionation within sulfide grains between mss and iss. Previously, Polyakov and Soultanov (2011) studied sulfides in term of their Fe β-factors. Beta-factors are defined as the ratio at equilibrium of the isotope ratio of the substance of interest to the isotope ratio of dissociated atoms (White, 2015). Beta-factor for troilite should be smaller (0.3) than in chalcopyrite (0.5), indicating that troilite should be depleted in heavy Fe isotopes compared to chalcopyrite (Polyakov and Soultanov, 2011), consistent with our results.

In summary, our results, including the relatively homogenous mineral composition (Section 4.1; Table 1), major and trace element compositions of sulfides (Table 2, Table S5–S9), as well as $\delta^{34}S$ (Fig. 5A and Table S14), $\delta^{65}Cu$ (Fig. 5B and Table S11), and $\delta^{56}Fe$ isotope signatures (Fig. 5C, Tables S12–S13), all indicate that magmatic processes formed the sulfides present throughout the igneous layering. The magmatic origin of sulfides presented in this study is consistent with observations of magmatic sulfides in the neighboring ODP Hole 735B (Alt and Anderson, 1991; Miller and Cervantes, 2002) located 2 km away from U1473A. Those sulfides, similar to ours, are polyphase and in many cases form globular grains enclosed in silicates.

5.2. Petrogenetic model of igneous layering formation

The strong enrichment of magmatic sulfides at the layer boundaries (Sections 4.1 and Fig. 2), prompts us to reconstruct how they formed, because the mechanism of sulfide enrichment may be intimately related to the nature of igneous layering in the Atlantis Bank lower oceanic crust. According to Dick et al., (2017) and Macleod et al., (2017), four possible processes for the origin of the Atlantis Bank igneous layering are: (1) melts migrating along zones of deformation; (2) processes related to crystal-plastic deformation; (3) focused melt flow (i.e., intrusion) through a crystal mush; and (4) reactive porous melt flow. Regarding the first process, the migrating melts along shear zones should yield sharp boundaries between the layers and mylonitic textures, or contact metamorphism on the walls of the host gabbroic rocks. However, we did not observe any of these features, and thus this process was rejected for further consideration. With regards to the second process, the fine- and coarse-grained layers do not show extensive crystal plastic deformation (MacLeod et al., 2017; Boulanger et al., 2021), and an origin by such a process is unlikely.

The third process, focused melt flow (i.e., intrusion) through a crystal mush, could be responsible for the igneous layering formation here. The boundaries between fine- and coarse-grained gabbros were sutured, which indicates the likely intrusive character of the fine-grained domains (e.g., see core sample 65R-5-0/5 on Figs. 2, S1 and S5; MacLeod et al., 2017). In addition, the early mush represented by the coarse-grained gabbro revealed a more evolved composition (Mg-numbers of 65 and 77 for Units II and VII, respectively) compared to the fine-grained gabbro (Mg-numbers of 69 and 79, respectively). This further suggests the existence of two different magma batches. Therefore, the newly injected melt likely intruded an earlier crystal mush, either by dissecting it, or meshing with it (for further discussion see Boulanger et al., 2021).

Considering the fourth process, many studies have demonstrated that reactive porous melt flow have played an important role in the formation of the lower oceanic crust (e.g., the Atlantis Bank, Kvassnes and Dick, 2000;

Gao et al., 2007; Lissenberg and MacLeod, 2016; Boulanger et al., 2020; Sanfilippo et al., 2020; (Ferrando et al., 2021b); the MAR, Coogan et al., 2000b; Lissenberg and Dick, 2008). Interactions between pre-existing cumulate minerals and migrating melts within the lower oceanic crust may form hybrid rocks characterized by distinct mineral and chemical compositions (Coogan et al., 2000a; Dick et al., 2002; Lissenberg and Dick, 2008; Lissenberg and MacLeod, 2016; Boulanger et al., 2020; Sanfilippo et al., 2020; Boulanger et al., 2021; Ferrando et al., 2021b). The observed sutured contacts, besides suggesting the intrusive character of the fine-grained domain, may have formed as a result of dissolution-reprecipitation processes along contacts between intruding melt and host rock (MacLeod et al., 2017). In our studied intervals, various features indicated that slightly more primitive melt (fine-grained gabbro; Table 3) reacted with partially consolidated crystal mush (coarse-grained gabbro) along the boundaries of different grain size layers. These features are: (1) formation of brown amphibole blebs associated with Fe-Ti oxides and sulfides both within and in the interstitial positions with clinopyroxene (Fig. 4E–H; Lissenberg and MacLeod, 2016; MacLeod et al., 2017); (2) occurrence of clinopyroxene–amphibole symplectites (Lissenberg and MacLeod, 2016; e.g., sample 13R-1-26/23); (3) lowered Mg-numbers on the rims of clinopyroxenes in the coarse-grained domain (Lissenberg and MacLeod, 2016; Boulanger et al., 2021; Ferrando et al., 2021b); and (4) common contact metamorphism at microscale, including fine-scale alteration of plagioclase to chlorite and green amphibole at its contact with the largest sulfides or oxides (Fig. 3).

The igneous layering studied herein were likely formed due to the intrusion of more primitive melts into the former crystal mush followed by the melt-rock reaction at the boundaries between these two domains. Although melt-rock reaction is not directly responsible for igneous layering formation here, it may affect sulfides, which are sensitive to even slight changes in the chemistry of mafic melts (Ciazela et al., 2017; Keith et al., 2017; Ciazela et al., 2018; Renna et al., 2020; Matusiak-Małek et al., 2021).

5.3. Mechanism of sulfide enrichment at the layer boundaries

Using macroscopic and petrographic features, supported by geochemical data, we have shown that fine-grained gabbros most likely represent an intrusion of slightly more primitive melt into a crystal mush (now the coarse-grained gabbro domains). Furthermore, we found sulfide enrichment along the layer boundaries. Most of these sulfides were associated with Fe-Ti oxides and brown amphibole in interstitial positions, which may indicate their late crystallization. However, injection of primitive magmas into a crystal mush does not explain itself the enhanced sulfide contents along the boundaries between coarse- and fine-grained gabbros. To further constrain the nature of the sulfide-enrichment process at the layer boundaries we determined the PGE contents of the sulfide grains. Experiments predict PGE fractionation during differentiation of sulfide liquid and distinguish the Ir-PGE (Ir, Os, Ru) and Pd-PGE (Pd, Pt, Rh) subgroups, based on their contrasting behavior. Whereas Ir-PGEs strongly partition to mss, Pd-PGEs show a higher affinity to iss (Barnes and Lightfoot, 2005; Holwell and McDonald, 2010; Fig. S9D). The ratio of Ir-PGEs and Pd-PGEs is controlled by various factors, including the degree of partial melting in the mantle, and the stage of magma evolution (Barnes and Lightfoot, 2005). Therefore, despite a similar magmatic source, as evidenced from the $\delta^{34}S$, $\delta^{65}Cu$, and $\delta^{56}Fe$ signatures, the PGE pattern allows for distinguishing two different magma batches. Our analyses revealed that sulfides from the coarse-grained gabbro are Ir-PGE-rich, but those from the fine-grained gabbro are Pd-PGE-rich (Fig. 6; Table S7–S9). Importantly, the sulfides of the layer boundaries are also enriched in Pd-PGEs, showing affinity to those from the fine-grained gabbro (Fig. 6). In addition, coarse-grained gabbro has a relatively flatter pattern compared to both fine-grained gabbro and layer boundaries (Fig. 6). Barnes and Lightfoot, (2005) as well as Patkó et al. (2021) showed that Fe-rich sulfides tend to have flatter normalized metal patterns, whereas the Cu-rich sulfides have steeper patterns due to the partitioning of PGEs to different sulfide phases. This seems to be consistent with the composition of our sulfides. The coarse-grained gabbros contain 90% pyrrhotite, 1% pentlandite, and only 9% chalcopyrite, whereas the layer boundaries are characterized by lower pyrrhotite mode (average of 84%), similar pentlandite mode (1%), and higher chalcopyrite mode (15%). We also found that all samples exhibit negative Pt anomalies (Fig. 6). Although Wirth et al. (2013) showed that Pt could be hosted by microalloys enclosed within the pyrrhotite and pentlandite, Holwell and McDonald (2010) demonstrated that Pt forms discrete platinum group minerals or is incorporated in electrum around the margins of sulfide grains. Although we did not find such microalloys using microscope or SEM, we cannot exclude their presence in our samples, especially at the sulfide margins.

These observations lead us to propose a petrogenetic model leading to the observed sulfide enrichment (Fig. 7). At first, the crystallizing mush (currently represented by the coarse-grained gabbro) composed of >80 vol.% crystals and <20 vol.% melt (cf. Lissenberg et al., 2019) (Fig. 7A) is intruded by a batch of slightly more primitive MORB magma (see Mg-number values in Table 3; Fig. 7B). The new magma partially crystallizes to form a fine-grained mush (Fig. 7C). Grain size difference is observed between the two lithologies, with much smaller crystals in the late narrow intrusions arising because the new melt's partially cooled environment is cooled faster than the earlier, slowly-cooling, coarse-grained material (Boulanger et al., 2021; Ferrando et al., 2021b). This is valid also for sulfides as we observed grain-size variations between sulfides from the coarse- and fine-grained domains (Section 4.1). Although the fine-grained gabbros contain more sulfide, the sulfide grains are relatively small.

From this point on, two complementary processes likely occur, leading to the enhanced sulfide precipitation along the boundaries. In the first process, both intruding partially crystallized melt and the former crystal mush suffer compaction and melt extraction required to account for whole-rock incompatible element signatures typical of a

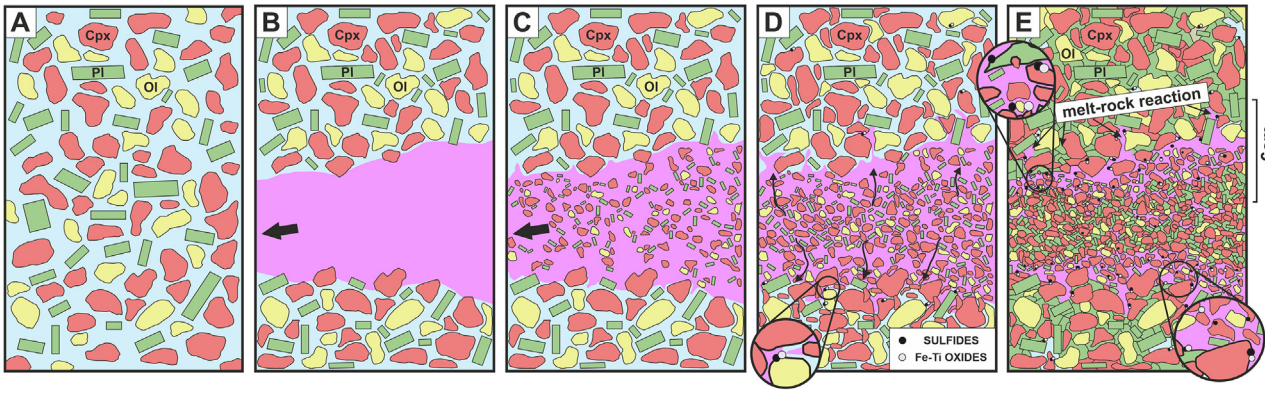

Fig. 7. Petrogenetic model of enrichment in sulfides along igneous layering boundaries between fine- and coarse-grained gabbros. At first, the crystallizing mush (A) is intruded by a melt (B). The intruding melt partially crystallizes to form a fine-grained mush (C). Subsequently, upon compaction, the melt can be preferentially extracted to the channel margins characterized by high textural heterogeneities at the grain size gradient (D). In a dry MORB crystallization sequence, Fe-oxides reach their saturation level only when the melt fraction is <23% (Feig et al., 2006). The subsequent Fe-Ti-oxide crystallization causes Fe loss from the melt and lowers the S concentration at sulfide saturation level (Ariskin et al., 2013). This results in sulfide crystallization next to oxides (E). Iron content in the melt is additionally lowered due to extensive Fe-Mg exchange-reaction on the rims of clinopyroxene (Cpx) and olivine (Ol), as evidenced by abundant sulfides at the rims of iron-bearing silicates, compared to plagioclase (Pl) (E).

cumulative origin (evidenced, for example, by the depleted rare earth element contents of the whole rocks compared to MORB-melts, and more specifically by the positive Eu anomalies which are especially pronounced for the lower and less distinct for the upper intervals; Fig. S7). At the decimeter-scale, the efficiency of melt migration increases with the permeability of the mush and is controlled by the average porosity, grain size and crystals shape (Hunter, 1996; Coogan et al., 2000a). Thus, textural heterogeneities at the interface, between crystallizing mushes, provide a viable melt path (Fig. 7D). In a dry MORB crystallization sequence, Fe-oxides saturates relatively late when the remaining melt fraction is low (<23%; Feig et al., 2006) (Fig. 7D). Iron-titanium-oxides are therefore expected to crystallize from a percolating or trapped late melt. The crystallization of Fe-Ti-oxides likely caused Fe loss in the melt, which in turn lowered the S concentration at the sulfide saturation level (cf. Ariskin et al., 2013) and resulted in sulfide crystallization next to oxides along the boundaries (Fig. 7E and S12).

In addition, the presence of the residual melt along the boundaries between the two domains might result in an extensive melt-rock reaction. The squeezed melt, concentrated along the boundaries, becomes relatively more evolved and reacts with the former crystal mush during percolation (Fig. 7D, Table 3). Then, the Fe concentration in the melt can be lowered again because of the Fe-Mg exchange-reaction between the melt and the rims of clinopyroxene and olivine. In fact, the rims of clinopyroxene exhibited lower Mg-number compared to their cores (Ferrando et al., 2021b). As a consequence, the S concentration at sulfide saturation level (Luguet et al., 2003; Ariskin et al., 2013) is locally lowered triggering the preferential crystallization of sulfide grains at the interstitial positions to clinopyroxenes and olivines (Figs. 7E and 4E–G).

The two described processes are likely complementary and might occur simultaneously, at least to some extent. Thus, they may have a synergetic effect in enhancing sulfide precipitation along the boundaries between the fine- and coarse-grained gabbro, which is especially the case for the upper interval. There, we infer relatively evolved melt composition (see relatively high REE, Fig. S7). This is likely responsible for abundant oxides (see Feig et al., 2006) that make up 70% of the opaque minerals. The high contribution of oxides in the upper interval is associated with high enrichment in sulfides suggesting the major role of Fe-Ti oxide crystallization for sulfide precipitation. In contrast, with little oxide in the lower interval (10% of the opaque minerals), which is consistent with more primitive magma composition (note high Mg-numbers (76–79) and low REE contents of the cumulates; Fig. S7), most Fe was lost from melt due to the Fe-Mg exchange reaction with silicate minerals. Consequently, the degree of enrichment in sulfides in the lower interval was relatively modest.

5.4. Local and global extent of sulfide enrichment zones in the lower oceanic crust

Copper enrichment along the layer boundaries may affect the local, and potentially global, Cu budget of the oceanic crust. Our local results (Section 4.2) indicate that all individual layer boundaries (5.7 ± 2.1 cm wide; 1SD) from the upper and lower intervals (Units II and VII) display Cu enrichment of 20–690% compared to the Unit II and VII averages (Table 3 and Section 4.2). On average, the boundary samples from the upper intervals contain 370% more Cu compared to the average for Unit II, whereas, in the lower interval, enrichment was only 50% (with reference to Unit VII). Despite certain differences, these observations prompt us to expect that all, or most, boundaries in U1473A are enriched in Cu. For example, an irregular boundary sampled by us in Unit VIII (thin-section 76R-3 86/93-CIAZ; Fig. S11) showed enhanced sulfide content of 0.44 vol.% determined by SEM MLA, which

would be an equivalent of 2493 ppm S. This would indicate enrichment of 293% with reference to Unit VIII (MacLeod et al., 2017).

Sulfur and Cu concentrations clearly correlate (Fig. S8) and appear to be controlled by the same process. We found that nearly all studied boundaries from Unit II and VII were enriched in S and Pb, in addition to Cu (Section 4.2). The layer boundaries between the fine- and coarse-grained gabbros constitute ~6.6% of Unit II and ~7.0% of Unit VII of the recovered magmatic core of the Hole U1473A (see Table 5), and the recovery rates were 59.6% and 95.6%, respectively (Table S16; Macleod et al., 2017). Based on the results presented in Section 4.2 and calculations in Table 5, we have estimated that an excess of ~19.5% and ~3.5% of the Cu, ~8.3% and ~0.4% of the S, and ~19.9% and ~83.6% of the Pb inventory in the oceanic crust could be accumulated at the layer boundaries in Units II and VII, respectively.

Our observations of the Cu enrichment related to igneous layering in U1473A are supported by the adjacent Hole 735B. Its upper parts contain intervals of fine-grained gabbros that show intrusive contacts with the surrounding very coarse-grained gabbros and resemble the igneous layering described herein. The fine-grained gabbro most likely represents an intrusion of a relatively primitive magma, as indicated by higher olivine modes (Miller and Cervantes, 2002). Similarly, in our study, the fine-grained gabbros exhibited a slightly more primitive composition (Mg-number of 69 and 79), compared to that of the coarse-grained gabbros (65 and 77; Sections 4.1 and 5.1). In Hole 735B, Miller and Cervantes (2002) analyzed a 5-cm-long interval (176-735B-123R-4, 106–111 cm; 744 mbsf), where fine-grained gabbro intrudes coarse-grained gabbro and found the highest sulfide abundances at the boundaries between the two gabbros. This matches our observations that a higher amount of sulfides were found along the igneous layering boundaries and within the fine-grained, slightly more primitive gabbros, compared to the coarse-grained gabbros (Section 4.1). A similar sulfide enrichment related to interlayered gabbroic rocks was found also in ODP Site 922, located on the western median valley of the MAR (Shipboard Scientific Party, 1995). Those sulfides were associated with Fe-Ti oxides, which are suggested to form during migration of late-stage melts (Natland et al., 1991; Dick et al., 2000; Natland and Dick, 2001; Koepke et al., 2018). The common genetic link between the sulfides and Fe-Ti oxides further supports our model that precipitation of oxides trigger sulfide crystallization along, at least in magmas related to the lower oceanic crust, slow-spreading ridges.

Igneous processes leading to enhanced sulfide precipitation due to melt-rock reaction might also occur at fast-spreading ridges. This is possible when new magma, with different chemistry, percolates through the former crust. This may be the case for the Semail Ophiolite. There, new magmas penetrated the former MORB-type crust, which could have been related either to partial melting of the shallow and partially hydrated lithosphere after MORB extraction (Python and Ceuleneer, 2003) or supra-subduction zone magmatism (Lachize et al., 1996; Goodenough et al., 2014). There, a disseminated sulfide-rich zone was found in the upper parts of the layered gabbro section in the Wadi Haymiliyah (Haylyn Block; Lachize et al., 1991, 1996). Those lithologies are weakly affected by hydrothermal alteration and hence, magmatic textures are well preserved. Sulfides are observed as spherical grains enclosed in plagioclase and pyroxenes, or irregular interstitial grains, especially in the layers richest in sulfides (Lachize et al., 1991, 1996). In this section of layered gabbros, the sulfides are preferentially concentrated in the fine-grained two-pyroxene gabbro and boundaries, whereas the coarse-grained (olivine) gabbro is sulfide poor. Therefore, despite the different tectonic setting, a similar process to that presented in this study may be invoked.

The melt-rock reactions within the lower oceanic crust associated with sulfide enrichment might be common along slow-, and perhaps fast-spreading, ridges. However, studies of sulfides related to igneous layering remain limited. More extensive studies in Atlantis Bank, other OCCs, and ophiolites will be highly beneficial in the future.

5.5. Implications for chalcophile elements' mass balance of the lower oceanic crust

The chalcophile element enrichment identified at the boundaries between different grain size domains in the lower oceanic crust of a slow-spreading center likely affect the global mass balance for Cu, S, Pb, and perhaps other chalcophile elements. MORB differentiation within the oceanic reservoirs was previously thought to be mainly controlled by fractional crystallization (Grove et al., 1992). In typical MORB-like melts that reach sulfur saturation after 10% of fractional crystallization, the Cu content starts to linearly decrease upon MORB differentiation at MgO contents of <9 wt% (Jenner and O'Neill, 2012; Patten et al., 2013; Jenner et al., 2015; Jenner, 2017). This implies that sulfide-bearing lower-crust cumulates should be enriched in chalcophile elements compared to the overlaying dikes and lavas (Li, 2014; Ciazela et al., 2017). However, Coogan's (2014) global average Cu concentration for gabbro (MORB cumulates) is 71 ± 19 ppm, which is lower than expected, considering 100–120 ppm Cu in the primitive MORB (Jenner and O'Neill, 2012; Lee et al., 2012; Jenner, 2017), and 72–81 ppm Cu in MORBs (Engel et al., 1965; Hamlyn et al., 1985; Doe, 1994; White and Klein, 2013). This discrepancy had been already highlighted by Jenner (2017), Ciazela et al. (2017, 2018), and Wang et al. (2018). Ciazela et al. (2018) proposed an explanation for this deficit and suggested that 20–62% of the Cu load in a primitive melt could be lost either at the crust-mantle transition or in melt-modified mantle rocks in the upper mantle.

Here, we propose an alternative (or complementary) possibility to explain the Cu deficit in the oceanic crust. A certain portion of the Cu deficit could be "hidden" within the crust itself, and not only trapped in the upper mantle. Using our results for layer boundaries documented in Hole U1473A, we estimated to what extent layer boundaries may explain Cu deficit in the lower crust. We have taken into account three scenarios considering

Table 5
Estimation of the Cu, S, and Pb budgets in the Atlantis Bank lower oceanic crust for Units II and VII within which igneous layering was documented from Hole U1473A.

		Unit II		Unit VII	
Depth (mbsf)		91.3–175.0		577.7–642.0	
Total length of the unit (m)		83.7		64.3	
Average recovery rate (%)		59.6		95.6	
Total number of igneous boundaries within the unit		58[1]		76[1]	
		Regular core	Layer boundaries	Regular core	Layer boundaries
Cumulative length (m)		49.9[2]	3.3[3]	61.5[2]	4.3[3]
Average Cu content (ppm)		52[4]	243[5]	66[4]	100[5]
Excess Cu content (ppm)[7]			191		34
Contribution to the Cu budget[8]	(m × ppm)	2594	629	4057	146
	(%)	80.5	19.5	96.5	3.5
Average S content (ppm)		386[4]	915[5]	407.5[4]	432[5]
Excess S content (ppm)[7]			529		24.5
Contribution to the S budget[8]	(m × ppm)	19,256	1746	25,050	105
	(%)	91.7	8.3	99.6	0.4
Average Pb content (ppm)		2.5[6]	11.9[5]	2.5[6]	184.7[5]
Excess Pb content (ppm)[7]			9.4		182.2
Contribution to the Pb budget[8]	(m × ppm)	125	31	154	784
	(%)	80.1	19.9	16.4	83.6

The authors declare that they have no known competing financial interests or personal relationships that could have appeared to influence the work reported in this paper.

[1] Based on Fig. 12, MacLeod et al. (2017) reports ~128 grain size layers in 67 series, which implies 195 layer boundaries. As one series is on average composed of 1.91 layers and 2.91 layer boundaries, 38 layers reported in Unit 2 mean 58 layer boundaries, and 50 layers reported in Unit VII mean 76 layer boundaries.

[2] The total length of the unit times average recovery rate (e.g., 83.7 m × 59.6% = 49.9 m).

[3] Total number of igneous boundaries within the unit times average length of a boundary sample (5.7 ± 1.4 cm wide; 2SE; see Section 5.4) (e.g., 58 × 0.057 m = 3.3 m).

[4] The average metal content within the units calculated based on shipboard data of Expedition IODP 360 in MacLeod et al. (2017).

[5] The average metal content based on Table 3.

[6] Based on Table S15.

[7] The average content in the boundary minus the average content for regular core (e.g., 243 − 52 ppm = 191 ppm).

[8] The contribution to the metal budget has been calculated both for the regular core and layer boundary zones. For the regular core, we have multiplied the cumulative length and average metal content (e.g., 49.9 × 52 = 2594), while for the layer boundaries the excess content was multiplied with the cumulative length of layer boundaries (e.g., 3.3 × 191 = 629). Only the excess content is used to estimate the metal contribution of layered boundaries because a portion of a given metal in the layer boundaries is the background value (assumed to be an average content in the hole).

that MORB-like melts, and dikes with lavas contain (#1) 100 and 81 ppm Cu; (#2) 110 and 76.5 ppm Cu; (#3) 120 and 72 ppm Cu, respectively (see Section 1). For these scenarios, the lower crustal cumulates should contain 110, 127, and 144 ppm Cu (see Section 1 and Table S17) to compensate the discrepancy between the MORB-like melts and dikes with lavas (Li, 2014; Ciazela et al., 2017). Assuming that layer boundaries constitute ~5.4% (see notes in Table S17) of the lower crust at the slow-spreading settings, we calculated an average Cu content (taking as an input 172 ppm Cu) for the whole lower crust that increased from 71.0 (Coogan, 2014) to 76.4 ppm Cu explaining 9.6% of the Cu deficit (scenario #2; Table S17). If using the Cu averages determined only for Units II (243 ppm Cu) or only for Unit VII (100 ppm Cu), we would obtain 16.4% (80.2 ppm Cu) or 2.9% (on average 72.6 ppm Cu) of Cu deficit for the whole lower crust (scenario #2; Table S17). Considering other scenarios (Table S17), we calculated that Cu enrichment along layer boundaries might explain from ~2% up to ~24% of the Cu deficit for the lower crust. Ciazela et al. (2018) proposed that 20–80% of the Cu can be lost from the melt during reaction with mantle peridotite at the crust-mantle boundary and along melt channels in the upper mantle. This could explain 17–69% of the global Cu deficit in the lower crust. Combining those results for the melt-mantle reaction with our current results on melt-gabbro reaction, we conclude that melt-rock reaction explains from 19% (17% at crust-mantle and 2% at layer boundaries) to 93% (69% at crust-mantle and 24% at layer boundaries) of the global Cu deficit in the lower crust. Although our calculations are addressed only for the slow-spread oceanic crust, the fast-spread crust also shows igneous layering, where a similar enrichment mechanism could operate. There is still 7–81% that remains missing, and we guess they may be trapped within the dunite channels or pyroxenitic cumulates that commonly occur in the oceanic and continental mantle. However, this guess is so far confirmed only by elevated Cu contents (Wang et al., 2018; Chen et al., 2020) in the continental mantle and it needs yet to be verified for the oceanic mantle. Global mass balance for the oceanic lithosphere is based on a representative sampling of recovered cores. Although inspected by petrologists, the boundaries between different gabbro layers are rarely analyzed in shipboard whole-rock analyses. One quick way to overcome this could be systematic inspection of the boundaries during the routine shipboard magnetic susceptibility and X-ray fluorescence scannings. We think that some additional Cu might be unexplored within the lower crust and more detailed studies are needed to fully understand the chalcophile elements distribution and migration.

The role of reactive porous flow in controlling the mid-ocean ridge magmatic evolution is significant (Dick and Zhou, 2015; Lissenberg and MacLeod, 2016), which was also recently suggested for the continental crust (Jackson et al., 2018), volcanic arc (Cooper et al., 2016), and hotspot settings (Gleeson et al., 2021). Reactive melt flow may affect how chalcophile elements are controlled during MORB differentiation. We propose that decrease in the Cu concentrations displayed by global correlations attributed to fractional crystallization (Jenner and O'Neill, 2012; Jenner, 2017) does not always reflect local magma differentiation trends (c.f., Ciazela et al., 2017). Especially in slow-spreading ridges, the decrease or increase in Cu may depend on more heterogenous processes, including melt-rock reaction with early formed crystal mush or country rock. Therefore, we propose the distributions of Cu, S, Pb and other metals is highly heterogenous in the lower oceanic crust and that they are especially enriched in chalcophile elements along zones where enhanced melt-rock reactions occurred. Thus, igneous layering should be examined more systematically in the future to estimate how they affect the oceanic lithosphere mass balance of various chalcophile and siderophile metals.

6. CONCLUSIONS

1. Layer boundaries in the interlayered gabbroic units of the Atlantis Bank OCC are significantly enriched in sulfides and chalcophile elements. The igneous layering intervals from Units II and VII of IODP Hole U1473A reveal different intensities of enrichment, with Cu contents being 2–5 times higher than the average Cu content of rocks throughout the hole.
2. Mineralogy, texture, and chemical composition of the sulfides indicate a magmatic origin of the chalcophile element enrichment. These sulfides formed at the interfaces between crystal mushes and new intruding magmas of more primitive composition. The crystallization of sulfides along the boundaries of fine- and coarse-grained gabbros is driven by FeO depletion from the melt that is accompanied by lowering S concentration at sulfide saturation level. The iron loss may be related to: (1) Fe-Ti oxides precipitating late in the remaining melt pockets focused along the boundaries and (2) Fe-Mg exchange-reaction on the rims of clinopyroxene and olivine during reactive porous flow.
3. The enhanced precipitation of sulfide grains at the boundaries can affect the metal budget of the lower oceanic crust. We estimate that an excess of ~4–20% for Cu, ~0.4–8.3% for S, and ~20–84% for Pb inventory, could accumulate at the layer boundaries. As those intrusive contacts are rarely sampled for mass balance calculations, our result may explain why Cu contents are underestimated in global budgets of the oceanic crust, and of the lower oceanic crust itself.

Declaration of Competing Interest

The authors declare that they have no known competing financial interests or personal relationships that could have appeared to influence the work reported in this paper.

ACKNOWLEDGMENTS

We thank editor D. Teagle, A. Sanfilippo, W. Maier, and an anonymous reviewer for their thorough and insightful comments.

This research used samples and data provided by the International Ocean Discovery Program (IODP). IODP is sponsored by the U.S. National Science Foundation (NSF) and participating countries under management of the Consortium for Ocean Leadership (COL). We would like to thank the other Expedition 360 Scientists and the crew of *JOIDES Resolution*. We thank M. Rechowicz from the Polish Geological Institute – National Research Institute for preparing samples for the SHRIMP measurements, M. Sitnikova from the Bundesanstalt für Geowissenschaften und Rohstoffe for performing SEM MLA analysis, and C. Mandeville, N. Shimizu, A. Fiege from Woods Hole Oceanographic Institution for providing the Sudbury pyrrhotite standard. Further help was provided by A. Duczmal-Czernikiewicz and M. Nowak from the Adam Mickiewicz University, and F. Holtz from the Leibniz University of Hannover, for which we are grateful. This research was funded by National Science Centre Poland (PRELUDIUM 12 no. 2016/23/N/ST10/00288), Graduate Academy of the Leibniz Universität Hannover (60421784), and ECORD Research Grant to J. Ciazela, as well as Deutsche Forschungsgemeinschaft (KO1723/23-1) to J. Koepke and H. Strauss. J. Ciazela is additionally supported within the START program of the Foundation for Polish Science (FNP). This is CRPG contribution No. 2813.

APPENDIX A. SUPPLEMENTARY MATERIAL

Supplementary data to this article can be found online at https://doi.org/10.1016/j.gca.2022.01.004.

REFERENCES

Alt J. C. and Anderson T. F. (1991) Mineralogy and Isotopic Composition of Sulfur in Layer 3 Gabbros From the Indian Ocean, Hole 735B. In *Proceedings of the Ocean Drilling Program, Scientific Results, College Station, TX (Ocean Drilling Program)* (eds. R. P. Von Herzen and P. T. Robinson), pp. 113–125.

Alt J. C., Shanks W. C., Bach W., Paulick H., Garrido C. J. and Beaudoin G. (2007) Hydrothermal alteration and microbial sulfate reduction in peridotite and gabbro exposed by detachment faulting at the Mid-Atlantic Ridge, 15°20′N (ODP Leg 209): A sulfur and oxygen isotope study. *Geochem. Geophys. Geosyst.* **8**.

Ariskin A. A., Danyushevsky L. V., Bychkov K. A., McNeill A. W., Barmina G. S. and Nikolaev G. S. (2013) Modeling solubility of Fe-Ni sulfides in basaltic magmas: The effect of nickel. *Econ. Geol.* **108**, 1983–2003.

Baines A. G., Cheadle M. J., Dick H. J. B., Scheirer A. H., John B. E., Kusznir N. J. and Matsumoto T. (2003) Mechanism for generating the anomalous uplift of oceanic core complexes: Atlantis Bank, southwest Indian Ridge. *Geology* **31**, 1105–1108.

Ballhaus C. and Sylvester P. (2000) Noble metal enrichment processes in the Merensky Reef, Bushveld Complex. *J. Petrol.* **41**, 545–561.

Barnes S.-J. and Lightfoot P. C. (2005) Formation of magmatic nickel-sulfide ore deposits and processses affecting their copper and platinum-group element contents. *Econ. Geol.* **100**, 179–213.

Barnes S.-J., Naldrett A. J. and Gorton M. (1985) The origin of the fractionation of platinum-group elements in terrestrial magmas. *Chem. Geol.* **53**, 303–323.

Blackman D. K. and Collins J. A. (2010) Lower crustal variability and the crust/mantle transition at the Atlantis Massif oceanic core complex. *Geophys. Res. Lett.* **37**, 1–5.

Blum P., MacLeod C. J., Dick H. J. B., Abe N., Blackman D. K., Bowles J. A., Cheadle M. J., Cho K., Ciazela J., Deans J. R., Edgcomb V. P., Ferrando C., France L., Ghosh B., Ildefonse B. M., Kendrick M. A., Koepke J. H., Leong J. A. M., Liu C., Ma Q., Morishita T., Morris A., Natland J. H., Nozaka T., Pluemper O., Sanfilippo A., Sylvan J. B., Tivey M. A., Tribuzio R. and Viegas L. G. F. (2017) Hole U1473A remediation operations, Expedition 362T. In *Southwest Indian Ridge Lower Crust and Moho. Proceedings of the International Ocean Discovery Program, 360: College Station, TX (International Ocean Discovery Program)* (eds. C. J. MacLeod, H. J. B. Dick, P. Blum and Expedition 360 Scientists).

Bonatti E., Ligi M., Brunelli D., Cipriani A., Fabretti P., Ferrante V., Gasperini L. and Ottolini L. (2003) Mantle thermal pulses below the Mid-Atlantic Ridge and temporal variations in the formation of oceanic lithosphere. *Nature* **423**, 499–505.

Boudier F., Godard M. and Armbruster C. (2000) Significance of gabbronorite occurrence in the crustal section of the Semail ophiolite. *Mar. Geophys. Res.* **21**, 307–326.

Boulanger M., France L., Deans J. R. L., Ferrando C., Lissenberg C. J. and von der Handt A. (2020) Magma Reservoir Formation and Evolution at a Slow-Spreading Center (Atlantis Bank, Southwest Indian Ridge). *Front. Earth Sci.* **8**, 1–24.

Boulanger M., France L., Ferrando C., Ildefonse B., Ghosh B., Sanfilippo A., Liu C. Z., Morishita T., Koepke J. and Bruguier O. (2021) Magma-Mush Interactions in the Lower Oceanic crust: Insights from Atlantis Bank Layered Series (Southwest Indian Ridge). *J. Geophys. Res. Solid Earth* **126**, e2021JB022331.

Canfield D. E., Raiswell R., Westrich J. T., Reaves C. M. and Berner R. A. (1986) The use of chromium reduction in the analysis of reduced inorganic sulfur in sediments and shales. *Chem. Geol.* **54**, 149–155.

Cannat M. (1996) How thick is the magmatic crust at slow spreading oceanic ridges? Melt migration in the axial lithosphere of slow spreading ridges: constraints from ultramafic and gabbroic samples. *J. Geophys. Res. Solid Earth* **101**, 2847–2857.

Carignan J., Hild P., Mevelle G., Morel J. and Yeghicheyan D. (2001) Routine analyses of trace elements in geological samples using flow injection and low pressure on-line liquid chromatography coupled to ICP-MS: A study of geochemical reference materials BR, DR-N, UB-N, AN-G and GH. *Geostand. Geoanal. Res.* **25**, 187–198.

Castelain T., McCraig A. M. and Cliff R. A. (2014) Fluid evolution in an Oceanic Core Complex: A fluid inclusion study from IODP hole U1309 D – Atlantis Massif, 30°N, Mid-Atlantic Ridge. *Geochem. Geophys. Geosyst.* **15**, 1193–1214.

Chen K., Tang M., Lee C. T. A., Wang Z., Zou Z., Hu Z. and Liu Y. (2020) Sulfide-bearing cumulates in deep continental arcs: The missing copper reservoir. *Earth Planet. Sci. Lett.* **531** 115971.

Ciazela J., Dick H. J. B., Koepke J., Pieterek B., Muszynski A., Botcharnikov R. and Kuhn T. (2017) Thin crust and exposed mantle control sulfide differentiation in slow-spreading ridge magmas. *Geology* **45**, 935–938.

Ciazela J., Koepke J., Dick H. J. B., Botcharnikov R., Muszynski A., Lazarov M., Schuth S., Pieterek B. and Kuhn T. (2018) Sulfide enrichment at an oceanic crust-mantle transition zone: Kane Megamullion (23°N, MAR). *Geochim. Cosmochim. Acta* **230**, 155–189.

Ciazela J., Koepke J., Dick H. J. B. and Muszynski A. (2015) Mantle rock exposures at oceanic core complexes along mid-ocean ridges. *Geologos* **21**, 207–231.

Coogan L. A. (2014) *The Lower Oceanic Crust*, second ed. Elsevier, Amsterdam, Netherlands.

Coogan L. A., Kempton P. D., Saunders A. D. and Norry M. J. (2000a) Melt aggregation within the crust beneath the Mid-Atlantic Ridge: Evidence from plagioclase and clinopyroxene major and trace element compositions. *Earth Planet. Sci. Lett.* **176**, 245–257.

Coogan L. A., Saunders A. D., Kempton P. D. and Norry M. J. (2000b) Evidence from oceanic gabbros for porous melt migration within a crystal mush beneath the Mid-Atlantic Ridge. *Geochem. Geophys. Geosyst.* **1**, 2000GC000072.

Cooper G. F., Davidson J. P. and Blundy J. D. (2016) Plutonic xenoliths from Martinique, Lesser Antilles: evidence for open system processes and reactive melt flow in island arc crust. *Contrib. Mineral. Petrol.* **171**, 1–21.

Craddock P. R., Warren J. M. and Dauphas N. (2013) Abyssal peridotites reveal the near-chondritic Fe isotopic composition of the Earth. *Earth Planet. Sci. Lett.* **365**, 63–76.

Dauphas N., Craddock P. R., Asimow P. D., Bennett V. C., Nutman A. P. and Ohnenstetter D. (2009) Iron isotopes may reveal the redox conditions of mantle melting from Archean to Present. *Earth Planet. Sci. Lett.* **288**, 255–267.

Delacour A., Früh-Green G. L. and Bernasconi S. M. (2008) Sulfur mineralogy and geochemistry of serpentinites and gabbros of the Atlantis Massif (IODP Site U1309). *Geochim. Cosmochim. Acta* **72**, 5111–5127.

Dick H. J. B., Kvassnes A. J. S., Robinson P. T., MacLeod C. J. and Kinoshita H. (2019a) The Atlantis Bank Gabbro Massif, Southwest Indian Ridge. *Prog. Earth Planet. Sci.* **6**.

Dick H. J. B., MacLeod C. J., Blum P., Abe N., Blackman D. K., Bowles J. A., Cheadle M. J., Cho K., Ciazela J., Deans J. R., Edgcomb V. P., Ferrando C., France L., Ghosh B., Ildefonse B., John B., Kendrick M. A., Koepke J., Leong J. A. M., Liu C., Ma Q., Morishita T., Morris A., Natland J. H., Nozaka T., Pluemper O., Sanfilippo A., Sylvan J. B., Tivey M. A., Tribuzio R. and Viegas G. (2019b) Dynamic Accretion Beneath a Slow-Spreading Ridge Segment: IODP Hole 1473A and the Atlantis Bank Oceanic Core Complex. *J. Geophys. Res. Solid Earth* **124**, 12631–12659.

Dick H. J. B., MacLeod C. J., Blum P., Abe N., Blackman D. K., Bowles J. A., Cheadle M. J., Cho K., Ciazela J., Deans J. R., Edgcomb V. P., Ferrando C., France L., Ghosh B., Ildefonse B. M., Kendrick M. A., Koepke J. H., Leong J. A. M., Liu C., Ma Q., Morishita T., Morris A., Natland J. H., Nozaka T., Pluemper O., Sanfilippo A., Sylvan J. B., Tivey M. A., Tribuzio R. and Viegas L. G. F. (2017) Expedition 360 summary. In *Proceedings of the International Ocean Discovery Program 360: College Station, TX (International Ocean Discovery Program)* (eds. C. J. MacLeod, H. J. B. Dick, P. Blum and Expedition 360 Scientists).

Dick H. J. B., MacLeod C. J., Blum P. and Expedition 360 Scientists (2016) Expedition 360 Preliminary report: Southwest Indian Ridge lower crust and Moho. *Int. Ocean Discov. Progr.*. doi.10.14379/iodp.pr.360.2016.

Dick H. J. B., Natland J. H. and Ildefonse B. (2006) Past and Future Impact of Deep Drilling in the Oceanic Crust and Mantle. *Oceanography* **19**, 72–80.

Dick H. J. B., Natland J. H., Jay M. D., Alt J. C., Bach W., Bideau D., Gee J. S., Haggas S., Hertogen J. G. H., Hirth G., Holm P. M., Isledefonse B., Iturrino G. J., John B. E., Kelley D. S., Kikawa E., Kingdon A., LeRoux P. J., Maeda J., Meyer P. S., Richard N. H., Niu Y.-L., Robinson P. T., Snow J., Stephen R. A., Trimby P. W., Wörm H.-U. and Yoshinobu A. (2000) A long in situ section of the lower ocean crust: Results of ODP leg 176 drilling at the Southwest Indian Ridge. *Earth Planet. Sci. Lett.* **179**, 31–35.

Dick H. J. B., Ozawa K., Meyer P. S., Niu Y., Robinson P. T., Constantin M., Hebert R., Maeda J. and Natland James.H., Hirth J. G. and Mackie S. M. (2002) Primary silicate mineral chemistry of a 1.5-km section of very slow spreading lower ocean crust: ODP Hole 753B, Southwest Indian Ridge. In *Proceedings of the Ocean Drilling Praogram: Scientific Results* (eds. J. H. Natland, H. J. B. Dick, D. J. Miller and R. P. Von Herzen).

Dick H. J. B. and Zhou H. (2015) Ocean rises are products of variable mantle composition, temperature and focused melting. *Nat. Geosci.* **8**, 68–74.

Dilek Y. (2003) Ophiolite concept and its evolution. *Spec. Pap. Soc. Am.* **373**, 1–16.

Doe B. R. (1994) Zinc, copper, and lead in mid-ocean ridge basalts and the source rock control on Zn/Pb in ocean-ridge hydrothermal deposits. *Geochim. Cosmochim. Acta* **58**, 2215–2223.

Durazzo A. and Taylor L. A. (1982) Exsolution in the mss-pentlandite system: Textural and genetic implications for Ni-sulfide ores. *Miner. Depos.* **17**, 313–332.

Engel A. E. J., Engel C. G. and Havens R. G. (1965) Chemical Characteristics of Oceanic Basalts and the Upper Mantle. *Geol. Soc. Am. Bull.* **7**, 719–734.

Escartín J., Smith D. K., Cann J., Schouten H., Langmuir C. H. and Escrig S. (2008) Central role of detachment faults in accretion of slow-spreading oceanic lithosphere. *Nature* **455**, 790–794.

Expedition 304/305 Scientists (2006) Site U1309. In *Proceedings of the Integrated Ocean Drilling Program, Volume 304/305: College Station TX (Integrated Ocean Drilling Program Management International, Inc.)* (eds. D. K. Blackman, B. Ildefonse, B. E. John, Y. Ohara, D. J. Miller, C. J. MacLeod and Expedition 304/305 Scientists).

Fandrich R., Gu Y., Burrows D. and Moeller K. (2007) Modern SEM-based mineral liberation analysis. *Int. J. Miner. Process.* **84**, 310–320.

Feig S. T., Koepke J. and Snow J. E. (2006) Effect of water on tholeiitic basalt phase equilibria: An experimental study under oxidizing conditions. *Contrib. Miner. Pet.* **152**, 611–638.

Ferrando C., Basch V., Ildefonse B., Deans J., Sanfilippo A., Barou F. and France L. (2021a) Role of compaction in melt extraction and accumulation at a slow spreading center: Microstructures of olivine gabbros from the Atlantis Bank (IODP Hole U1473A, SWIR). *Tectonophysics* **815** 229001.

Ferrando C., France L., Basch V., Sanfilippo A., Tribuzio R. and Boulanger M. (2021b) Grain size variations record segregation of melts residual from reactive migration in slow-spreading oceanic crust (Atlantis Bank; 57°E Southwest Indian Ridge). *J. Geophys. Res.-Solid Earth* **126**, e2020JB020997.

Fiege A., Holtz F., Shimizu N., Mandeville C. W., Behrens H. and Knipping J. L. (2014) Sulfur isotope fractionation between fluid and andesitic melt: An experimental study. *Geochim. Cosmochim. Acta* **142**, 501–521.

France L., Ildefonse B. and Koepke J. (2009) Interactions between magma and hydrothermal system in Oman ophiolite and in IODP Hole 1256D: Fossilization of a dynamic melt lens at fast spreading ridges. *Geochem. Geophys. Geosyst.* **10**, 1–30.

Francis C. A., Fleet M. E., Misra K. and Craig J. R. (1976) Orientation of exsolved pentlandite in natural and synthetic nickeliferous pyrrhotite. *Am. Mineral.* **61**, 913–920.

Gao Y., Hoefs J., Hellebrand E., von der Handt A. and Snow J. E. (2007) Trace element zoning in pyroxenes from ODP Hole 735B gabbros: Diffusive exchange or synkinematic crystal fractionation? *Contrib. Mineral. Petrol.* **153**, 429–442.

Gleeson M. L. M., Gibson S. A. and Stock M. J. (2021) Upper Mantle Mush Zones beneath Low Melt Flux Ocean Island Volcanoes: Insights from Isla Floreana, Galápagos. *J. Petrol.* **61**, 1–26.

Godard M., Awaji S., Hansen H., Hellebrand E., Brunelli D., Johnson K., Yamasaki T., Maeda J., Abratis M., Christie D., Kato Y., Mariet C. and Rosner M. (2009) Geochemistry of a long in-situ section of intrusive slow-spread oceanic lithosphere: Results from IODP Site U1309 (Atlantis Massif, 30°N Mid-Atlantic-Ridge). *Earth Planet. Sci. Lett.* **279**, 110–122.

González-Jiménez J. M., Proenza J. A., Pastor-Oliete M., Saunders E., Aiglsperger T., Pujol-Solà N., Melgarejo J. C., Gervilla F. and Garcia-Casco A. (2020a) Precious metals in magmatic Fe-Ni-Cu sulfides from the Potosí chromitite deposit, eastern Cuba. *Ore Geol. Rev.* **118** 103339.

González-Jiménez J. M., Tassara S., Schettino E., Roqué-Rosell J., Farré-de-Pablo J., Saunders J. E., Deditius A. P., Colás V., Rovira-Medina J. J., Dávalos M. G., Schilling M., Jimenez-Franco A., Marchesi C., Nieto F., Proenza J. A. and Gervilla F. (2020b) Mineralogy of the HSE in the subcontinental lithospheric mantle — An interpretive review. *Lithos* **372–373** 105681.

Goodenough K. M., Thomas R. J., Styles M. T., Schofield D. I. and MacLeod C. J. (2014) Records of ocean growth and destruction in the Oman-UAE ophiolite. *Elements* **10**, 109–114.

Govindaraju K. and Mevelle G. (1987) Fully automated dissolution and separation methods for inductively coupled plasma atomic emission spectrometry rock analysis. Application to the determination of rare earth elements: Plenary lecture. *J. Anal. At. Spectrom.* **2**, 615–621.

Grove T. L., Kinzler R. J. and Bryan W. B. (1992) Fractionation of Mid-Ocean Ridge Basalt (MORB). In *Mantle Flow and Melt Generation at Mid-Ocean Ridges, Geophysical Monograph Series. Washington* (eds. J. P. Morgan, D. K. Blackman and J. M. Sinton), pp. 281–310.

Guillong M., Meier D. L., Allan M. M., Heinrich C. A. and Yardley B. W. D. (2008) SILLS: A Matlab-Based Program for the Reduction of Laser Ablation ICP–MS Data of Homogeneous Materials and Inclusions. *Mineral. Assoc. Canada Short Course* **40**, 328–333.

Hamlyn P. R., Keays R. R., Cameron W. E., Crawford A. J. and Waldron H. M. (1985) Precious metals in magnesian low-Ti lavas: Implications for metallogenesis and sulfur saturation in primary magmas. *Geochim. Cosmochim. Acta* **49**, 1797–1811.

Holwell D. A. and McDonald I. (2010) A review of the behaviour of platinum group elements within natural magmatic sulfide ore systems. *Platin. Met. Rev.* **54**, 26–36.

Horn I. and von Blanckenburg F. (2007) Investigation on elemental and isotopic fractionation during 196 nm femtosecond laser ablation multiple collector inductively coupled plasma mass spectrometry. *Spectrochim Acta – Part B At. Spectrosc.* **62**, 410–422.

Horn I., von Blanckenburg F., Schoenberg R., Steinhoefel G. and Markl G. (2006) In situ iron isotope ratio determination using UV-femtosecond laser ablation with application to hydrothermal ore formation processes. *Geochim. Cosmochim. Acta* **70**, 3677–3688.

Hunter R. H. (1996) Texture Development in Cumulate Rocks. In *Cawthorn Layered Intrusions* (ed. R. G. Cawthorn). Elsevier, pp. 77–101.

Ildefonse B., Blackman D., John B. E., Ohara Y., Miller D. J., MacLeod C. J., Abe N., Abratis M., Andal E. S., Andréani M., Awaji S., Beard J. S., Brunelli D., Charney A. B., Christie D. M., Delacour A. G., Delius H., Drouin M., Einaudi F., Escartin J., Frost B. R., Fryer P. B., Gee J. S., Godard M., Grimes C. B., Halfpenny A., Hansen H. E., Harris A. C., Hasebe A. T., Hayman N. W., Hellebrand E., Hirose T., Hirth J. G., Ishimaru S., Johnson K. T. M., Karner G. D., Linek M., Maeda J., Mason O. U., McCaig A. M., Michibayashi K., Morris A., Nakagawa T., Nozaka T., Rosner M., Searle R. C., Suhr X., Tominaga M., von der Handt A., Yamasaki T. and Zhao X. (2006) IODP expeditions 304 & 305 Characterize the Lithology, Structure, and Alteration of an Oceanic Core Complex. *Sci. Drill.* **1**, 4–11.

Jackson M. D., Blundy J. and Sparks R. S. J. (2018) Chemical differentiation, cold storage and remobilization of magma in the Earth's crust. *Nature* **564**, 405–409.

Jenner F. E. (2017) Cumulate causes for the low contents of sulfide-loving elements in the continental crust. *Nat. Geosci.* **10**, 524–529.

Jenner F. E., Hauri E. H., Bullock E. S., König S., Arculus R. J., Mavrogenes J. A., Mikkelson N. and Goddard C. (2015) The competing effects of sulfide saturation versus degassing on the behavior of the chalcophile elements during the differentiation of hydrous melts. *Geochem. Geophys. Geosyst.* **16**, 1490–1507.

Jenner F. E. and O'Neill H. S. C. (2012) Analysis of 60 elements in 616 ocean floor basaltic glasses. *Geochem. Geophys. Geosyst.* **13**, 1–11.

Jenner F. E., O'Neill H. S. C., Arculus R. J. and Mavrogenes J. A. (2010) The magnetite crisis in the evolution of arc-related magmas and the initial concentration of Au, Ag and Cu. *J. Petrol.* **51**, 2445–2464.

Kajiwra Y. and Krouse H. R. (1971) Sulfur isotope partitioning in metallic sulfide systems. *Earth Sci.* **8**, 1397–1408.

Kaneda H., Takenouchi S. and Shoji T. (1986) Stability of pentlandite in the Fe-Ni-Co-S system. *Miner. Depos.* **21**, 169–180.

Keith M., Haase K. M., Klemd R., Schwarz-Schampera U. and Franke H. (2017) Systematic variations in magmatic sulphide chemistry from mid-ocean ridges, back-arc basins and island arcs. *Chem. Geol.* **451**, 67–77.

Kissin S. A. and Scott S. D. (1982) Phase relations involving pyrrhotite below 350 degrees C. *Econ. Geol.* **77**, 1739–1754.

Klein E. M. (2003) Geochemistry of the igneous ocean crust. In *Treatise on Geochemistry Vol. 3, The Crust* (ed. R. L. Rudnick), pp. 433–463.

Koepke J., Botcharnikov R. E. and Natland J. H. (2018) Crystallization of late-stage MORB under varying water activities and redox conditions: Implications for the formation of highly evolved lavas and oxide gabbro in the ocean crust. *Lithos* **323**, 58–77.

Koepke J., Feig S. and Snow J. (2005) Late stage magmatic evolution of oceanic gabbros as a result of hydrous partial melting: Evidence from the Ocean Drilling Program (ODP) Leg 153 drilling at the Mid-Atlantic Ridge. *Geochem. Geophys. Geosyst.* **6**, Q02001.

Kvassnes A. and Dick H. J. (2000) Deviations from dry fractionation trends in gabbros from Atlantis Bank, South West Indian Ocean. *EOS. Trans. Am. Geophys Union* **82**.

Lachize M., Lorand J. P. and Juteau T. (1996) Calc-alkaline differentiation trend in the plutonic sequence of the Wadi Haymiliyah section, Haylayn massif, Semail ophiolite, Oman. *Lithos* **38**, 207–232.

Lachize M., Lorand J. P. and Juteau T. (1991) Cu-Ni-PGE Magmatic Sulfide Ores and their Host Layered Gabbros in the Haymiliyah Fossil Magma Chamber (Haylayn Block, Semail Ophiolite Nappe, Oman). *Ophiolite Genes. Evol. Ocean. Lithosph.* **5**, 209–229.

Larson P. B., Maher K., Ramos F. C., Chang Z., Gaspar M. and Meinert L. D. (2003) Copper isotope ratios in magmatic and hydrothermal ore-forming environments. *Chem. Geol.* **201**, 337–350.

Lazarov M. and Horn I. (2015) Matrix and energy effects during in-situ determination of Cu isotope ratios by ultraviolet-femtosecond laser ablation multicollector inductively coupled plasma mass spectrometry. *Spectrochim. Acta – Part B At. Spectrosc.* **111**, 64–73.

Lee C. T. A., Luffi P., Chin E. J., Bouchet R., Dasgupta R., Morton D. M., Le Roux V., Yin Q. Z. and Jin D. (2012) Copper systematics in Arc Magmas and Implications for Crust-Mantle Differentiation. *Science (80-.)* **335**, 64–66.

Li R., Xia X. P., Chen H., Wu N., Zhao T., Lai C., Yang Q. and Zhang Y. (2020) A Potential New Chalcopyrite Reference Material for Secondary Ion Mass Spectrometry Sulfur Isotope Ratio Analysis. *Geostand. Geoanal. Res.* **44**, 485–500.

Li Y. (2014) Chalcophile element partitioning between sulfide phases and hydrous mantle melt: Applications to mantle melting and the formation of ore deposits. *J. Asian Earth Sci.* **94**, 77–93.

Li Y. and Liu J. (2006) Calculation of sulfur isotope fractionation in sulfides. *Geochim. Cosmochim. Acta* **70**, 1789–1795.

Lissenberg C. J. and Dick H. J. B. (2008) Melt-rock reaction in the lower oceanic crust and its implications for the genesis of mid-ocean ridge basalt. *Earth Planet. Sci. Lett.* **271**, 311–325.

Lissenberg C. J. and MacLeod C. J. (2016) A reactive porous flow control on mid-ocean ridge magmatic evolution. *J. Petrol.* **57**, 2195–2220.

Lissenberg J. C., MacLeod C. J. and Bennett E. N. (2019) Consequences of a crystal mush-dominated magma plumbing system: A mid-ocean ridge perspective. *Philos. Trans. R. Soc. A* **377**.

Lissner M., König S., Luguet A., le Roux P. J., Schuth S., Heuser A. and le Roex A. P. (2014) Selenium and tellurium systematics in MORBs from the southern Mid-Atlantic Ridge (47–50°S). *Geochim. Cosmochim. Acta* **144**, 379–402.

Liu S. A., Huang J., Liu J., Wörner G., Yang W., Tang Y. J., Chen Y., Tang L., Zheng J. and Li S. (2015) Copper isotopic composition of the silicate Earth. *Earth Planet. Sci. Lett.* **427**, 95–103.

Lorand J. P. and Juteau T. (2000) The Haymiliyah sulphide ores (Haylayn massif, Oman phiolite): In-situ segregation of PGE-poor magmatic sulphides in a fossil oceanic magma chamber. *Mar. Geophys. Res.* **21**, 327–349.

Luguet A., Lorand J. P. and Seyler M. (2003) Sulfide petrology and highly siderophile element geochemistry of abyssal peridotites: A coupled study of samples from the Kane Fracture Zone (45° W 23°20N, MARK area, Atlantic Ocean). *Geochim. Cosmochim. Acta* **67**, 1553–1570.

MacLeod C. J., Dick H. J. B., Blum P., Abe N., Blackman D. K., Bowles J. A., Cheadle M. J., Cho K., Ciazela J., Deans J. R., Edgcomb V. P., Ferrando C., France L., Ghosh B., Ildefonse B. M., Kendrick M. A., Koepke J. H., Leong J. A. M., Liu C., Ma Q., Morishita T., Morris A., Natland J. H., Nozaka T., Pluemper O., Sanfilippo A., Sylvan J. B., Tivey M. A., Tribuzio R. and Viegas L. G. F. (2017) Site U1473A. In *Proceedings of the International Ocean Discovery Program, 360: College Station, TX (International Ocean Discovery Program)* (eds. C. J. MacLeod, H. J. B. Dick, P. Blum and Expedition 360 Scientists).

Malitch K. N., Latypov R. M., Yu I. and Sluzhenikin S. F. (2014) Insights into ore genesis of Ni-Cu-PGE sulfide deposits of the Noril'sk Province (Russia): Evidence from copper and sulfur isotopes. *Lithos* **204**, 172–187.

Matusiak-Małek M., Puziewicz J., Nta T., Woodland A., Uenverthiele L., Büchner J., Grégoire M. and Aulbach S. (2021) Variable origin of clinopyroxene megacrysts carried by Cenozoic volcanic rocks from the eastern limb of Central European Volcanic Province (SE Germany and SW Poland). *Lithos* **383** 105936.

McDonough W. F. and Sun S. S. (1995) The composition of the Earth. *Chem. Geol.* **120**, 223–253.

Miller J. and Cervantes P. (2002) Sulfide mineral chemistry and petrography and platinum group element composition in gabbroic rocks from the Southwest Indian Ridge. In *Proceedings of the Ocean Drilling Program, 176 Scientific Results* (eds. J. H. Natland, H. J. B. Dick, D. J. Miller and R. P. Von Herzen).

Mondal S. K. (2011) Platinum group element (PGE) geochemistry to understand the chemical evolution of the Earth's mantle. *J. Geol. Soc. India* **77**, 295–302.

Natland J. H. and Dick H. J. B. (2001) Formation of the lower ocean crust and the crystallization of gabbroic cumulates at a very slowly spreading ridge. *J. Volcanol. Geotherm. Res.* **110**, 191–233.

Natland J. H., Meyer P. S., Dick H. J. B. and Bloomer S. H. (1991) Magmatic Oxides and Sulfides in Gabbroic Rocks from Hole 735B and the Later Development of the Liquid Line of Descent. In *Proceedings of the Ocean Drilling Program, 118 Scientific Results, College Station, TX (Ocean Drilling Program)* (eds. R. Von Herzen and P. T. Robinson).

Nguyen D. K., Morishita T., Soda Y., Tamura A., Ghosh B., Harigane Y., France L., Liu C., Natland J. H., Sanfilippo A., Macleod C. J., Blum P. and Dick H. J. B. (2018) Occurrence of felsic rocks in oceanic gabbros from IOPD Hole 1473A: Implications for evolved melt migration in the lower oceanic crust. *Minerals* **8**, 583.

Nicolas A., Boudier F. and France L. (2009) Subsidence in magma chamber and the development of magmatic foliation in Oman ophiolite gabbros. *Earth Planet. Sci. Lett.* **284**, 76–87.

Oeser M., Strauss H., Wolff P. E., Koepke J., Peters M., Garbe-Schönberg D. and Dietrich M. (2012) A profile of multiple sulfur isotopes through the Oman ophiolite. *Chem. Geol.* **312–313**, 27–46.

Ozawa K., Meyer P. S. and Bloomer S. H. (1991) 3. Mineralogy and textures of iron-titnium oxide gabbros and associated olivine gabbros from Hole 735B. In *Proceedings of the Ocean Drilling Program, 118 Scientific Results, College Station, TX (Ocean Drilling Program)* (eds. R. P. Von Herzen and P. T. Robinson), pp. 41–73.

Palmiotto C., Corda L., Ligi M., Cipriani A., Dick H. J. B., Douville E., Gasperini L., Montagna P., Thil F., Borsetti A. M., Balestra B. and Bonatti E. (2013) Nonvolcanic tectonic islands in ancient and modern oceans. *Geochem. Geophys. Geosyst.* **14**, 4698–4717.

Patkó L., Ciazela J., Aradi L. E., Liptai N., Pieterek B., Berkesi M., Lazarov M., Kovács I. J., Holtz F. and Szabó C. (2021) Iron isotope and trace metal variations during mantle metasomatism: In situ study on sulfide minerals from peridotite xenoliths from Nógrád-Gömör Volcanic Field (Northern Pannonian Basin). *Lithos*, 396–397.

Patten C., Barnes S. J., Mathez E. A. and Jenner F. E. (2013) Partition coefficients of chalcophile elements between sulfide and silicate melts and the early crystallization history of sulfide liquid: LA-ICP-MS analysis of MORB sulfide droplets. *Chem. Geol.* **358**, 170–188.

Peters B. J., Shahar A., Carlson R. W., Day J. M. D. and Mock T. D. (2019) A sulfide perspective on iron isotope fractionation during ocean island basalt petrogenesis. *Geochim. Cosmochim. Acta* **245**, 59–78.

Peters M., Strauss H., Farquhar J., Ockert C., Eickmann B. and Jost C. L. (2010) Sulfur cycling at the Mid-Atlantic Ridge: A multiple sulfur isotope approach. *Chem. Geol.* **269**, 180–196.

Polyakov V. B. and Soultanov D. M. (2011) New data on equilibrium iron isotope fractionation among sulfides: Constraints on mechanisms of sulfide formation in hydrothermal and igneous systems. *Geochim. Cosmochim. Acta* **75**, 1957–1974.

Pouchou J.-L. and Pichoir F. (1991) Quantitative Analysis of Homogeneous or Stratified Microvolumes Applying the Model "PAP". In *Electron Probe Quantitation* (eds. K. F. J. Heinrich and D. E. Newbury). Springer, Boston, pp. 31–75.

Python M. and Ceuleneer G. (2003) Nature and distribution of dykes and related melt migration structures in the mantle section of the Oman ophiolite. *Geochem. Geophys. Geosyst.* **4**, 1–34.

Renna M. R., Armandola S., Becker H., Sanfilippo A., Tribuzio R. and Wang Z. (2020) Fractionation of highly siderophile and chalcogen elements in the lower oceanic crust: Insights from the troctolites of the Alpine-Apennine Jurassic ophiolites. *Lithos* **105873**.

Rice C. A., Tuttle M. L. and Reynolds R. L. (1993) The analysis of forms of sulfur in ancient sediments and sedimentary rocks: comments and cautions. *Chem. Geol.* **107**, 83–95.

Ripley E. M. and Li C. (2003) Sulfur isotope exchange and metal enrichment in the formation of magmatic Cu-Ni-(PGE) deposits. *Econ. Geol.* **98**, 635–641.

Ripley E. M., Li C., Moore C. H., Elswick E. R., Maynard J. B., Paul R. L., Sylvester P., Seo J. H. and Shimizu N. (2011) Analytical methods for sulfur determination in glasses, rocks, minerals and fluid inclusions. *Rev. Mineral. Geochem.* **73**, 9–39.

Rouxel O., Shanks W. C., Bach W. and Edwards K. J. (2008) Integrated Fe- and S-isotope study of seafloor hydrothermal vents at East Pacific Rise 9–10°N. *Chem. Geol.* **252**, 214–227.

Sanfilippo A., MacLeod C. J., Tribuzio R., Lissenberg C. J. and Zanetti A. (2020) Early-Stage Melt-Rock Reaction in a Cooling Crystal Mush Beneath a Slow-Spreading Mid-Ocean Ridge (IODP Hole U1473A, Atlantis Bank, Southwest Indian Ridge). *Front. Earth Sci.* **8** 579138.

Sanfilippo A., Morishita T. and Senda R. (2016) Rhenium-osmium isotope fractionation at the oceanic crust-mantle boundary. *Geology* **44**, 167–170.

Savage P. S., Moynier F., Chen H., Shofner G., Siebert J., Badro J. and Puchtel I. S. (2015) Copper isotope evidence for large-scale sulphide fractionation during Earth's differentiation. *Geochem. Perspect. Lett.*, 53–64.

Seal R. R. (2006) Sulfur Isotope Geochemistry of Sulfide Minerals. *Rev. Mineral. Geochem.* **61**, 633–677.

Shanks W. C. (2013) Stable Isotope Geochemistry of Mineral Deposits. In *Treatise on Geochemistry: Second Edition* (eds. H. D. Holland and K. K. Turekian). Elsevier, pp. 59–85.

Shipboard Scientific Party (1999a) Hammer Drill Site (1104 and 1106) and Site 1105. In *Proc. ODP, Init. Repts., 179: College Station, TX (Ocean Drilling Program)* (eds. T. L. Pettigrew, J. F. Casey and D. J. Miller), pp. 1–183.

Shipboard Scientific Party (1999b) Leg 179 summary. In *Proc. ODP, Init. Repts., 179: College Station, TX (Ocean Drilling Program)* (eds. T. L. Pettigrew, J. F. Casey and D. J. Miller), pp. 1–26.

Shipboard Scientific Party (1999c) Site 735. In *Proc. ODP, Init. Repts., 176: College Station, TX (Ocean Drilling Program)* (eds. H. J. B. Dick, J. H. Natland and D. J. Miller), pp. 1–314.

Shipboard Scientific Party (1995) Site 922. In *Proc. ODP, Init. Repts., 153: College Station, TX (Ocean Drilling Program)* (eds. M. Cannat, J. A. Karson and D. J. Miller), pp. 179–215.

Tostevin R., Turchyn A. V., Farquhar J., Johnston D. T., Eldridge D. L., Bishop J. K. B. and McIlvin M. (2014) Multiple sulfur isotope constraints on the modern sulfur cycle. *Earth Planet. Sci. Lett.* **396**, 14–21.

Vaughan D. J. and Corkhill C. L. (2017) Mineralogy of sulfides. *Elements* **13**, 81–87.

Wang Z., Becker H., Liu Y., Hoffmann E., Chen C., Zou Z. and Li Y. (2018) Constant Cu/Ag in upper mantle and oceanic crust: Implications for the role of cumulates during the formation of continental crust. *Earth Planet. Sci. Lett.* **493**, 25–35.

White W. M. (2015) Stable Isotope Theory. In *Isotope Geochemistry* (ed. William M. White). John Wiley & Sons Ltd, pp. 244–277.

White W. M. and Klein E. M. (2013) Composition of the Oceanic Crust. In *Treatise on Geochemistry: Second Edition* (eds. H. D. Holland and K. K. Turekian). Elsevier, pp. 457–496.

Wirth R., Reid D. and Schreiber A. (2013) Nanometer-sized platinum-group minerals (PGM) in base metal sulfides: New evidence for an orthomagmatic origin of the Merensky Reef PGE ore deposit, Bushveld Complex, South Africa. *Can. Mineral.* **51**, 143–155.

Wu H., He Y., Teng F. Z., Ke S., Hou Z. and Li S. (2018) Diffusion-driven magnesium and iron isotope fractionation at a gabbro-granite boundary. *Geochim. Cosmochim. Acta* **222**, 671–684.

Zhang W.-Q., Liu C.-Z. and Dick H. J. B. (2020) Evidence for Multi-stage Melt Transport in the Lower Ocean Crust: Atlantis Bank Gabbroic Massif (IODP Hole U1473A, SW Indian Ridge). *J. Petrol.* **61**, egaa082.

Zhou M. F., Robinson P. T., Malpas J., Aitchison J., Sun M., Bai W. J., Hu X. F. and Yang J. S. (2001) Melt/mantle interaction and melt evolution in the Sartohay high-Al chromite deposits of the Dalabute ophiolite NW China. *J. Asian Earth Sci.* **19**, 517–534.

Zhou M. F., Robinson P. T., Malpas J. and Li Z. (1996) Podiform chromitites in the Luobusa ophiolite (Southern Tibet): Implications for melt-rock interaction and chromite segregation in the upper mantle. *J. Petrol.* **37**, 3–21.

Zhu X. K., O'Nions R. K., Guo Y., Belshaw N. S. and Rickard D. (2000) Determination of natural Cu-isotope variation by plasma-source mass spectrometry: Implications for use as geochemical tracers. *Chem. Geol.* **163**, 139–149.